Introduction to the Physics of Membranes

Christoph A. Haselwandter
California Institute of Technology
cah77@caltech.edu

3/3/2010

These lecture notes provide a brief introduction to the physics of biological membranes, with a particular focus on the connection between the physical properties of membranes and the overall shapes of vesicles and cells. No attempt is made at carrying out a complete survey of this vast topic, which lies at the intersection of such disparate fields as topology, differential geometry, elasticity theory, statistical physics, thermodynamics, biochemistry, structural biology, and cell biology, to name just a few. Our discussion is based primarily on Refs. [1–3].

Contents

Chapter 1

Phenomenology of membranes

This chapter provides an introduction to the basic phenomenology of biological membranes, and the vesicles and cells obtained by closing up membranes to form continuous surfaces with no boundaries. Section 1.1 discusses the structure of membranes, while Sec. 1.2 points at the great diversity observed in the overall shapes of vesicles and cells.

1.1 The structure of membranes

Biological membranes are one of the most important hallmarks of life. They separate the cellular contents from the external environment, and thereby establish the spatial boundary of life, separating "animate" from "inanimate" matter. From a practical perspective, membranes must be able to maintain vast differences in chemical composition between the cell and its surroundings but, at the same, also allow the passage of nutrients into the cell and the passage of waste products out of the cell. Moreover, all communication of cells with the outside world passes through cell membranes in one form or the other and, hence, membranes need to allow for the flow of information. Finally, while membranes must be mechanically stable enough to withstand a hostile environment, the function and growth of cells is intimately tied to their shape and, thus, membranes must be sufficiently malleable to allow cell growth, cell division, and dynamic changes of cell shape. All of this has to be achieved in a reproducible manner. Thus, membranes must be able to reconcile a dazzling array of partly contradictory demands.

What material is able to satisfy the design specifications outlined above? Promising candidates are found among chemical compounds known as surfactants (surface active agents), exhibiting attractive interactions between different chemical substances which, by themselves, are effectively immiscible. Soap, for instance, consists of a polar headgroup, which is soluble in water, and a "water-avoiding" hydrocarbon chain. Thus, soap is an amphiphilic molecule able to dissolve tiny oil droplets in water. Cell membranes, however, are exposed to water on either side of the membrane. Thus, we are looking for surfactants which spontaneously assemble into bilayers, with their hydrophobic tails pointing inwards and their hydrophilic heads pointing outwards (see Fig. 1.1).

For the cell to work efficiently, and the cell membrane to be stable, the self-assembly of bilayers must be able to operate in solutions containing very low surfactant concentrations. Surfactants which satisfy this requirement can be found among a class of molecules known as *lipids* and, indeed, lipids turn out to be a basic building block of membranes. Although there exists a great variety of different lipids (more than 1000 different types of lipids have been identified in cells), the membranes of all cells contain lipids sharing the same basic molecular architecture. In particular, the polar headgroup of lipids is easily incorporated into the hydrogen-bonding network of the surrounding water, occupies

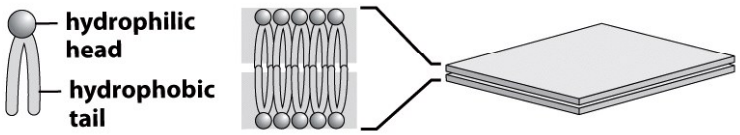

Figure 1.1: Schematic illustration of amphiphilic molecules and their possible arrangement into bilayers. (After Ref. [3].)

around 0.4–0.7 nm^2 in the bilayer, and has a thickness of typically around 0.5 nm. The hydrophobic part of lipids generally consists of two fatty acid chains, made up of 15–18 repeating units of CH_2 groups. At a length of approximately 0.1 nm per CH_2 group, each hydrocarbon chain has a total length of around 2 nm. This length of hydrocarbon chains thereby reflects the operating temperature of the cell so that, while the chains must be long enough to ensure efficient expulsion from water and stability of the bilayer, they must also be short enough to allow malleability of membranes. An exception to the bilayer architecture of membranes are archea, which feature a monolayer of bolalipids consisting of one long hydrocarbon chain and two polar headgroups.

Bilayers *versus* micelles

While the bilayer is an attractive arrangement for amphiphilic lipids, it is not the only large-scale arrangement one can imagine. In particular, as illustrated in Fig. 1.2, spheres or cylinders, the interiors of which are filled by the hydrophobic tails of lipids, are alternative possibilities. A more exotic arrangement are inverted micelles, such as shown in Fig. 1.2, for which the headgroups point towards the inside of the micelle. Can one understand the competition between the bilayer and other large-scale arrangements on the basis of the molecular architecture of lipids alone? We will address this question below using molecular packing arguments and find that, on a heuristic level, the large-scale arrangement of lipids can be deduced from a dimensionless quantity known as the shape factor $S = v_{\rm hc}/(a_0 l_{\rm hc})$, where $v_{\rm hc}$ is the volume of hydrocarbon chains, a_0 is the headgroup area, and $l_{\rm hc}$ is the chain length.

First note that, if the radius of the spherical micelle displayed in Fig. 1.2 is equal to R, we determine the number of lipids contained in the micelle as $4\pi R^2/a_0$ from the micelle surface area, and as $4\pi R^3/(3v_{\rm hc})$ from the micelle volume[1]. For these estimates to be consistent, we need $R = 3v_{\rm hc}/a_0$, while we must also have $R \leq l_{\rm hc}$. Thus, for

$$S \lessapprox 1/3 \tag{1.1}$$

lipids are able to self-organize into spherical micelles. However, to accommodate lipids with larger hydrocarbon tails, spherical micelles must distort to form ellipsoids. In an extreme case, the micelle will distort into a cylinder of radius R which, in a slice of thickness t contains $\pi R^2 t/v_{\rm hc} = 2\pi R t/a_0$ lipids, which gives $R = 2v_{\rm hc}/a_0$. Thus, we estimate that for

$$1/3 \lessapprox S \lessapprox 1/2 \tag{1.2}$$

distorted micelles will occur, with the lower bound obtained from the previous calculation. For single-tailed lipids one finds $S \approx 0.4$ and, thus, such lipids are expected to form distorted micelles.

[1]The boundary of the sphere approximating the micelle is defined as the neutral surface of bending, *i.e.*, the surface of constant area under bending. For lipid monolayers, one can approximate the neutral surface of bending by the surface sweeped out by the points joining the polar headgroups and the hydrocarbon tails of lipid molecules.

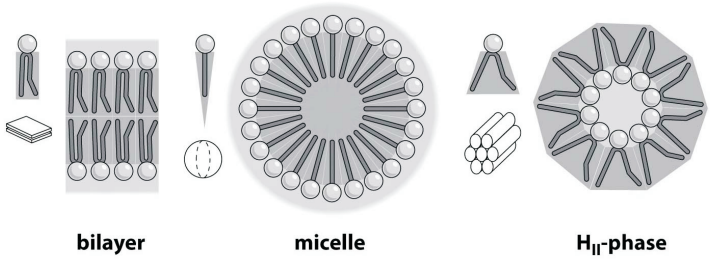

Figure 1.2: Coarse-grained representation of different lipid geometries, and their effect on the large-scale arrangement of lipids. (After Ref. [3].)

As the shape factor increases beyond 1/2, lipid tails are no longer able to pack into objects with curvature[2] corresponding to the inverse of the lipid tail length. Thus, larger-scale structures will become favorable. In particular, as S approaches 1, we have $v_{\rm hc} \to a_0 l_{\rm hc}$, which corresponds to lipids which have equal head and base areas. Thus, for

$$1/2 \lessapprox S \lessapprox 1 \tag{1.3}$$

we expect lipids to self-assemble into bilayers. Lipids with two hydrocarbon tails have $S \approx 0.8$ and, thus, it is reasonable that such lipids form bilayers, as is indeed observed. Moreover, also note that lipids with two hydrocarbon tails will be less likely to dissolve in water due to their larger hydrophobic surface area. This further facilitates the formation of lipid bilayers even at low lipid concentrations. Finally, as S increases beyond 1, lipids are expected to form structures such as inverted micelles.

Heterogeneity of biological membranes

Contrary to the simple picture presented above, biological membranes do not only consist of one type of lipid, but generally contain a variety of different lipid species which are distinguished, for instance, by the lengths of their hydrophobic tails, the charges on their headgroups, or whether hydrocarbon chains contain only single C-C bonds or also some double C-C bonds. Saturated hydrocarbons (single bonds) tend to straighten out when lipids form bilayers, whereas unsaturated hydrocarbons (double bonds) generate a kink in the carbon tail, which makes the dense packing of lipids more difficult and thereby reduces the in-plane viscosity of membranes. Other (more special) lipid molecules, such as cholesterol, can fill the gaps formed by kinks, and thereby compensate for unsaturated carbon bonds as far as the mechanical properties of membranes are concerned. Such changes in the physical properties of biological membranes can have profound consequences for their biological function.

In addition to a variety of different lipids, biological membranes also contain membrane proteins, which are crucial for the more sophisticated biological functions carried out by membranes. In fact, proteins typically make up most of the mass of biological membranes, and their mean spacing can be estimated to be only around 4 nm. Thus, the composition of biological membranes is generally very heterogeneous. In a classic cartoon representation [see Fig. 1.3(A)], the membrane is pictured as a two-dimensional fluid in which proteins can diffuse more or less freely in the plane of the membrane, but cannot move out of the plane. Further refinements of this cartoon [see Fig. 1.3(B)] emphasize crowding of molecules in membranes, the possibility of phase separation by both lipids and proteins in order to minimize membrane deformations, and the coupling between lipid and protein domains.

[2]We will define geometrical concepts such as "curvature" later on in these notes.

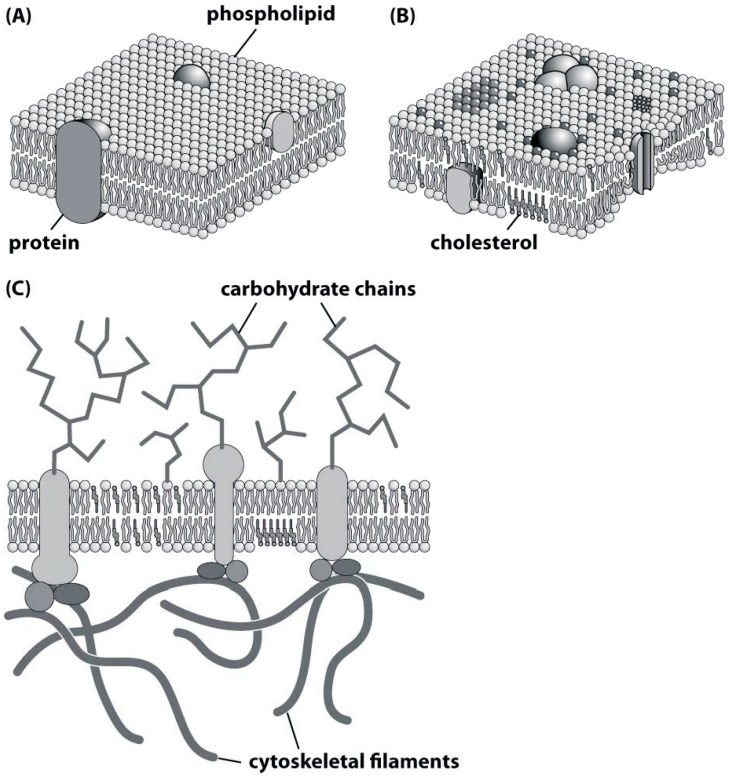

Figure 1.3: Classic cartoon representation of the structure of membranes [panel (A)], and its refinements [panels (B) and (C)]. (After Ref. [3].)

Finally, membrane properties might also be influenced by objects located outside the plane of the membrane [see Fig. 1.3(C)], such as the cytoskeleton of the cell, or domains of membrane proteins which protrude above neighboring parts of the membrane and thereby make them inaccessible.

1.2 Vesicles and cells

In the preceding section we discussed the phenomenology governing the self-assembly of lipid bilayers. But how do lipid bilayers self-organize at even larger scales to form vesicles or cells, which can be more than six orders of magnitude larger than the size of individual lipid molecules? Key to answering this question is an understanding of the physical principles driving the energetics of large bilayer structures. As we shall discuss in detail later in these notes, the large-scale behavior of closed vesicles is mostly determined by the energetic cost associated with bending the bilayer membrane. In the simplest description of vesicles, this energetic cost takes a constant value independent of the size of the vesicle. The boundaries of an open bilayer sheet, however, introduce an energetic cost which is proportional to the length of the boundary. Thus, on simple energetic grounds, we expect that for bilayers of large enough area it will be energetically favorable to close up into vesicles and, thus, to form the basis for cellular life.

Bilayer vesicles

Figure 1.4 shows a series of images of a bilayer vesicle taken taken at different temperatures. For the lowest temperatures considered, the bilayer vesicle has a simple spherical shape. But, as the

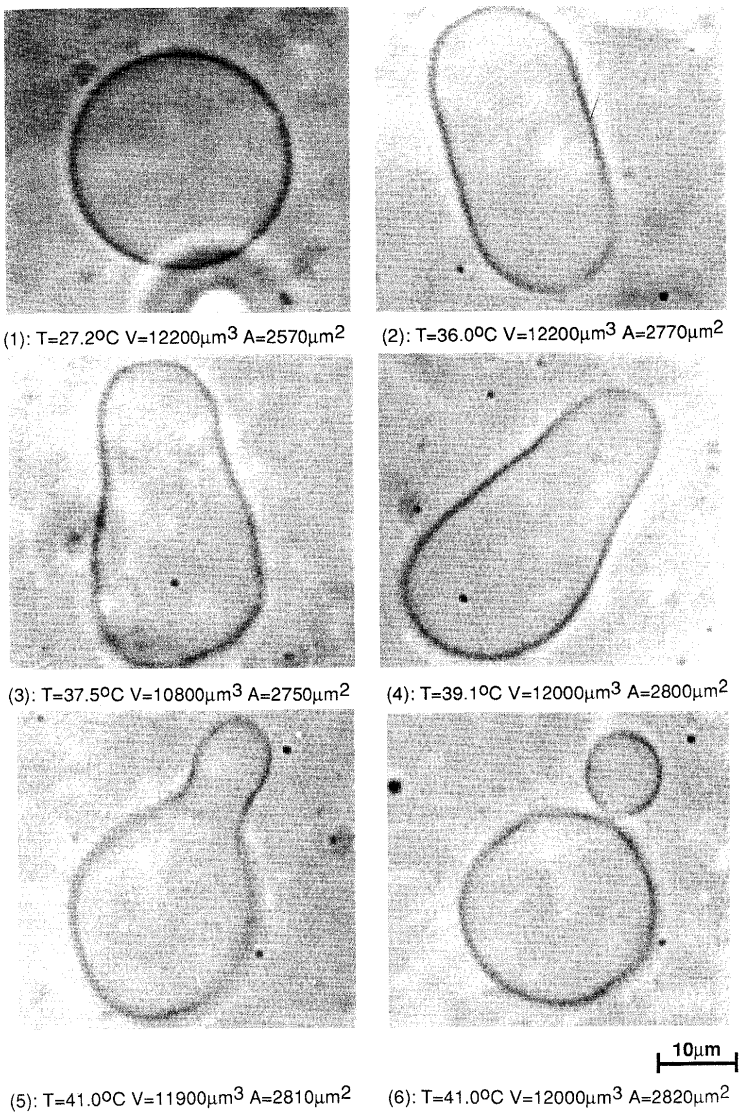

Figure 1.4: Budding transition of a bilayer vesicle. (After Ref. [4].)

temperature is increased, the vesicle shape becomes increasingly rod-like (the technical term being prolate ellipsoid). Considering that the vesicle area is increased at the higher temperature, whereas the solution is chosen so that the vesicle volume remains essentially unchanged, this might not be too surprising. However, as the temperature is increased even further, the symmetry of the shape is broken again, and the vesicle is increasingly pear-shaped. Finally, at even higher temperatures, the neck closes and we return to a similar shape as at the lowest temperature considered, but now, apparently, with two spherical vesicles instead of one. In fact, although not visible from the image, the two spherical compartments in the highest-temperature image are connected by a narrow bilayer cylinder.

The "budding transition" described above, which is somewhat reminiscent of the biological process of exocytosis, does, however, not always occur as the temperature is being increased. As shown in Fig. 1.5, the "up/down" reflection symmetry can also be restored among further heating, in which case no budding occurs. Moreover, instead of developing a rod-like shape, spherical vesicles can also

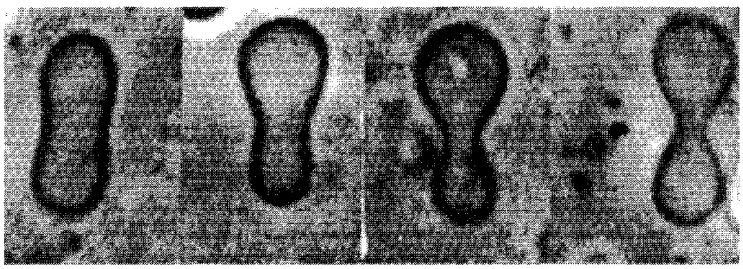

Figure 1.5: From left to right, the panels correspond to $T = 20.7, 32.6, 40.0$, and $44.3°$C, respectively. (After Ref. [5].)

acquire a pancake-shape (oblate ellipsoid) upon heating (see Fig. 1.6). Upon further heating, the vesicle then develops interesting shapes known as discocyte and stomatocyte, which will be discussed further in Sec. 3. These observations illustrate two essential physical properties of typical bilayer vesicles. First, the observed shape changes suggest that bilayer membranes are *fluid* in the sense that they do not resist shear. At the same time, however, the bilayer structure is also robust in the sense that no holes or formed and, while the spherical shape deforms significantly, the bilayers are not "cut" and "glued together" to form even more complicated shapes which could, presumably, be even more favorable from an energetic perspective. Indeed, the latter point is confirmed by carrying out similar experiments on vesicles as shown in Figs. 1.4–1.6 with a different topology (number of handles), such as tori, which are not observed to transform into spherical shapes.

All of the vesicle shapes described above are also exhibited by cells. For instance, Fig. 1.7 shows experimental images of red blood cells which, as the experimental conditions are varied, reliably reproduce the shapes in Fig. 1.6. Not too surprisingly, however, the extra layers of molecular complexity present in real cells allow the formation of even more intricate shapes, such as the so-called echinocyte shapes shown in the right three panels of Fig. 1.7. Broadening our scope, we note that biological cells come in a great variety of different shapes and sizes, such as illustrated in cartoon form in Fig. 1.8. A unified, predictive understanding of all of these cell shapes represents a daunting challenge, to say the least, and has so far not been achieved. However, given that all biological membranes share the same basic construction principles, one can contemplate meeting this challenge by gradually building up our systematic understanding of cell shape and size.

The above examples illustrate that even vesicles consisting of simple components (a single species of lipid molecules) are able to exhibit complicated shapes which are stable but can, nevertheless, be transformed from one shape to another in a reproducible manner as a function of well-defined variables such as temperature or chemical environment. This suggests that it might be possible to understand, at least to some degree, cell shape without invoking the full biochemistry of cells, such as complicated molecular machines. A vast body of work, relating the results of experiments to a systematic understanding of vesicle and cell shape in terms of physics, and *vice versa*, shows that

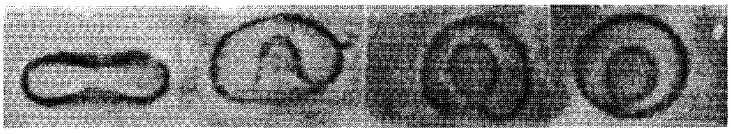

Figure 1.6: From left to right, the panels correspond to $T = 43.8, 43.9, 44.0$, and $44.1°$C, respectively. (After Ref. [5].)

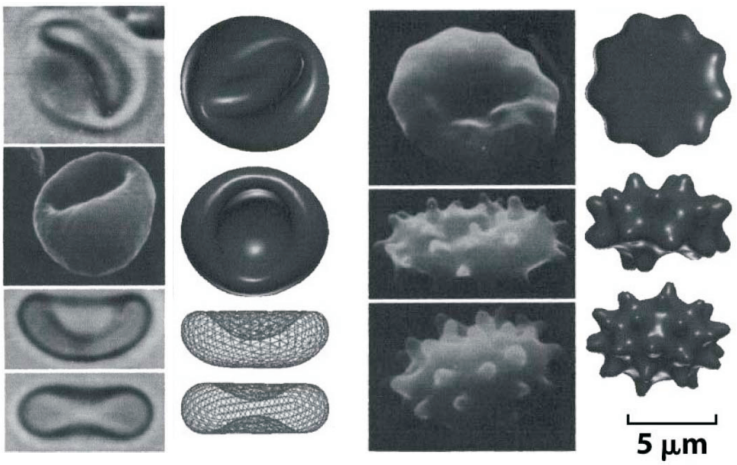

Figure 1.7: Representative shapes from the stomatocyte–discocyte–echinocyte sequence of red blood cells obtained from experiments (left images) and theory (right plots). See also Sec. 3.3. (After Ref. [6].)

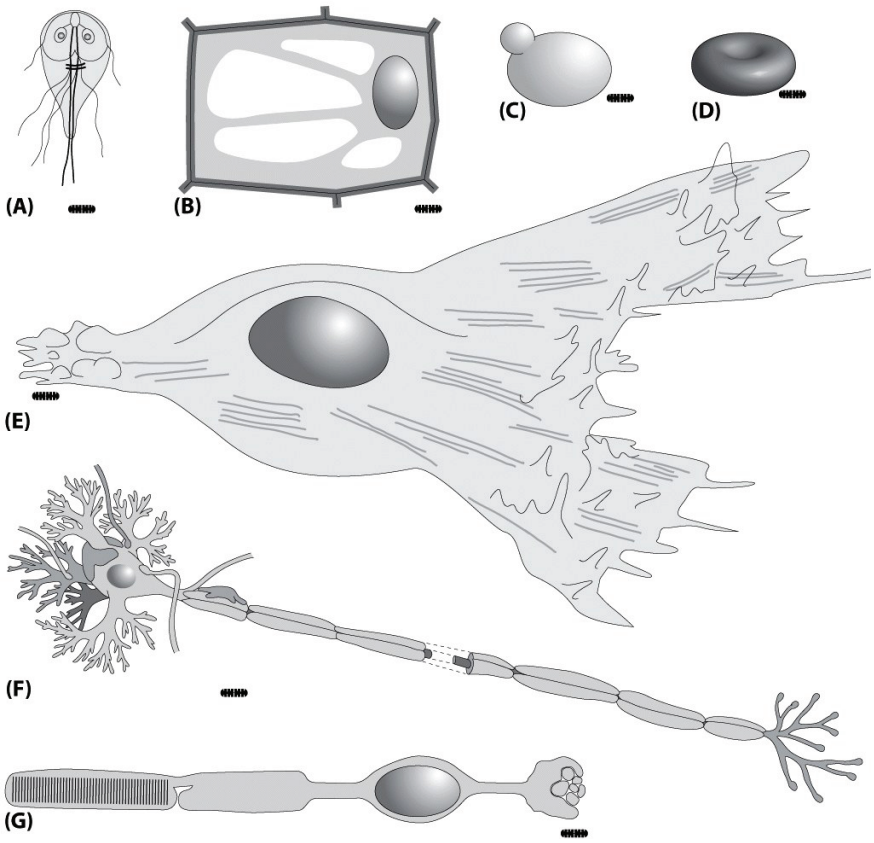

Figure 1.8: Schematic illustration of the great diversity in cell shape found in nature, with *E. coli*, which roughly has the shape of a cylinder of length 2 μm and thickness/height 1 μm, as a "measurement stick". For details, see Fig. 2.8 of Ref. [3]. (After Ref. [3].)

this is indeed the case. Importantly, such a quantitative understanding of cell and vesicle shape can be used to determine what classes of observed shapes require more complicated mechanisms beyond the basic physics of membranes. Moreover, a quantitative framework for understanding vesicle and cell shape allows the systematic testing of different, more complicated, mechanisms for the observed shapes by building on the basic phenomenology known from previous experiments. In these lecture notes, we will focus on the overall shape of vesicles and cells, and only consider the most basic "layer" of our understanding on which more complicated descriptions may be built. A similar approach can be (and, indeed, has been) applied to other aspects of biological membranes, such as the coupling between the properties of membranes and the proteins embedded in them. Finally, trivial as this point may seem, there is no reason to believe that not *all* aspects of living systems are amenable to the type of systematic reasoning and understanding illustrated here for biological membranes.

Chapter 2

Theory of membranes and vesicles

In this chapter we develop the basic physical and mathematical concepts which allow a systematic understanding of the shapes of membranes and vesicles. Section 2.1 discusses the major classes of membrane deformations. In many settings, bending deformations are found to dominate over other types of membrane deformations, and we will therefore discuss the physics of bending deformations in somewhat greater detail in Sec. 2.2. Finally, in Sec. 2.3 we develop the mathematical language appropriate for the quantitative discussion of membrane deformations and their consequences.

2.1 Membrane deformations

A useful starting point for the physical description of membranes is continuum elasticity theory, which is the classical mechanics of continuous media. In standard (discrete) mechanics, two fundamental quantities are the displacement of some mass from its equilibrium position, and the force associated with this displacement. In continuum mechanics, the two corresponding quantities are referred to as *strain* and *stress*, respectively. For a general three-dimensional system, strain and stress will be tensor rather than scalar quantities (for instance, the strain and stress tensors are often taken to be 3×3 matrices). Strain is a dimensionless quantity and corresponds to the spatial variation of the displacement vector characterizing the deformation of a continuous body. The (internal) stress tensor captures the (internal) forces which tend to return the body to its equilibrium arrangement, and its components have units of force per unit area along some appropriate axis. Thus, just as the motion of discrete bodies is determined by laws governing the relationship between displacement and force, the deformation properties of continuous bodies are determined, to a large extent, by the relationship between strain and stress.

Viewing membranes as continuous media, one can apply continuum elasticity theory to determine the energetic cost associated with arbitrary membrane deformations. While such a formal approach has undoubtedly many strengths, it will be more instructive for us to focus on the different types of membrane deformations which seem most relevant from a physical perspective, and to formulate, in the spirit of Taylor expansions, lowest-order descriptions for the elastic costs associated with these deformations. Our motivation for following this approach is as follows. From an experimental perspective, we are mainly interested in the dominant membrane deformations and their relative importance as a function of the specific experimental setup, rather than a complete treatment of the problem allowing for all possible membrane deformations. From a theoretical perspective, provided that our intuition has been "good" in the sense that we do indeed consider the dominant types of membrane deformations, such an approach allows us to do calculations without carrying any superfluous mathematical baggage. In particular, we will consider four different classes of membrane deformations, which are

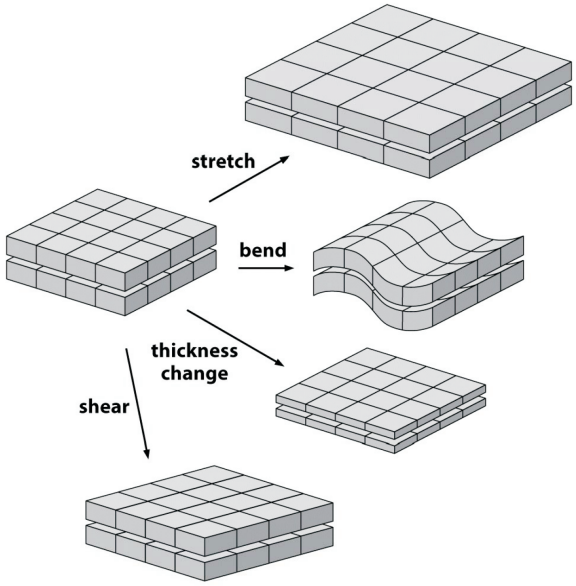

Figure 2.1: Illustration of four basic classes of membrane deformations. (After Ref. [3].)

illustrated in Fig. 2.1: changing the membrane area, bending, changing the membrane thickness, and shearing. These four types of deformations allow us to capture the basic phenomenology implied by the microscopic properties of membranes and their coupling to the environment, such as the particular types of lipids and proteins constituting the membrane, interactions of the membrane with an external cytoskeleton, and differing chemical conditions on the two sides of the membrane.

Changing the membrane area

Pulling along the sides of a membrane, we exert a *tension*, τ, or force per unit length, on the membrane. If the original state of the membrane corresponds to its equilibrium state, the tension will be opposed by the internal stress in the membrane (see Fig. 2.2). Following Hooke's law, the energetic cost of compressing or stretching a membrane is therefore given by

$$G_{\text{area}} = \frac{K_a}{2a_0}(\Delta a)^2\,, \tag{2.1}$$

where we have assumed that the change in membrane area Δa from the equilibrium area a_0 is homogeneous throughout the membrane, and K_a is a the area-stretch modulus with units of energy per unit area. Characteristic values of K_a fall in the range $K_a \approx 55$–$70 k_B T/\text{nm}^2$. The above expression can be generalized by including higher-order terms or allowing a spatial dependence of Δa.

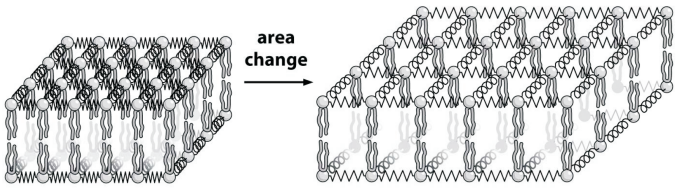

Figure 2.2: Illustration of the energetics associated with a change in membrane area. (After Ref. [3].)

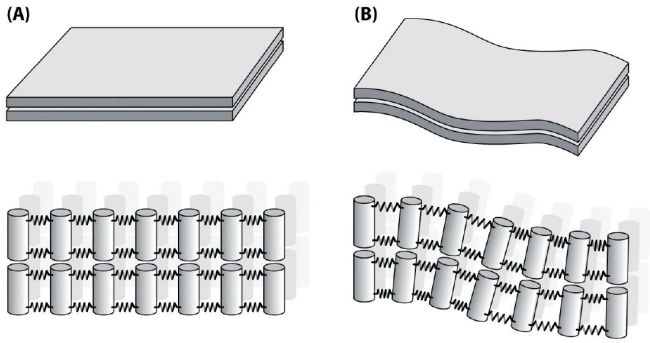

Figure 2.3: Illustration of the energetics of membrane bending. (After Ref. [3].)

Bending the membrane

Among the types of membrane deformations considered in Fig. 2.1, bending (see Fig. 2.3) turns out to be the dominant deformation for fluid lipid bilayers, and we therefore devote the next section exclusively to the bending of membranes. For now, we only note that the description of bending is intimately related to the concept of *curvature*, which will be discussed in greater detail in Sec. 2.3. We can characterize "how much" a membrane is bent at a particular point on the membrane by constructing a circle which just about follows the membrane in the direct vicinity of this point (see Fig. 2.4). The curvature is then defined as the inverse of this radius, with a positive or negative sign depending on whether the circle is drawn above or below the surface, which corresponds to the surface curving upward or downward, respectively. Thus, if the radius is very large (*i.e.*, the membrane is nearly flat in this particular direction), the curvature is small, and *vice versa*. As we shall see, the radius of such a circle touching the surface has a precise mathematical definition, and is referred to as an *osculating circle*. Furthermore, the minimal and maximal values of the radii of the osculating circles associated with a particular point on the membrane define the *principal curvatures*, C_1 and C_2, associated with this point. On this basis, one defines the *mean curvature*, H, and the *Gaussian*

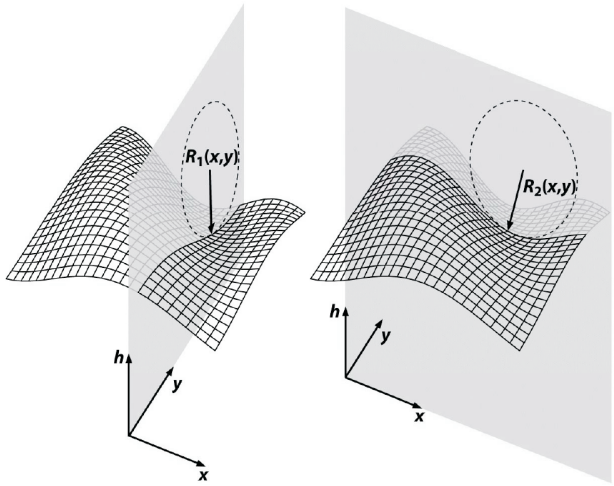

Figure 2.4: Illustration of osculating circles of radius R_1 and R_2, respectively. (After Ref. [3].)

curvature, G, as

$$H := \frac{1}{2}\left(C_1 + C_2\right) , \quad G := C_1 C_2 \, . \tag{2.2}$$

Thus, the mean curvature has dimensions of inverse length, and the Gaussian curvature has dimensions of inverse length squared.

We will show in Sec. 2.3 that physically meaningful quantities constructed from the radii of curvature can only depend on the values of H and G, respectively. Moreover, since in general the distinction between "up" and "down" when defining the curvature is arbitrary, only the square of the curvature can appear to lowest order (but see the next section). Thus, to lowest order, the bending energy must take the form

$$G_{\rm bend} = \frac{K_b}{2} \int dS H^2 + \frac{K_G}{2} \int dS G \, , \tag{2.3}$$

where the integral $\int dS$ is to be taken over the neutral surface along which the total contour area of the surface remains constant (see Fig. 2.3), and K_b and K_G are the bending rigidities associated with the mean and Gaussian curvatures, respectively. Typical values for the bending rigidity K_b are $K_b \approx 10$–$20 k_B T$ for fluid membranes. As will be discussed below, very little is known experimentally about the value (or even sign) of K_G, which is ultimately due to certain fundamental mathematical properties of surfaces. Finally, note from Fig. 2.1 that bending deformations are special in the sense that their description necessarily involves curved surfaces. Thus, we will need to employ differential geometry to give precise mathematical meaning to the various terms in Eq. (2.3). The relevant concepts will be developed in Sec. 2.3, and until then we will content ourselves with a more qualitative discussion of bending energy.

Changing the membrane thickness

Thickness changes are the "perpendicular analog" to the compression or expansion of the membrane area discussed above (see Fig. 2.5). In general, lipid bilayers and membrane proteins will have a mismatch in their hydrophobic thicknesses. Thus, the energetic cost associated with thickness changes is particularly relevant for the description of membrane proteins, and it is useful to allow a positional dependence of the membrane thickness, $\Delta w = w(x, y) - w_0$, where $2w_0$ is the equilibrium thickness of the membrane. To lowest order, the energy penalty associated with thickness deformations is again

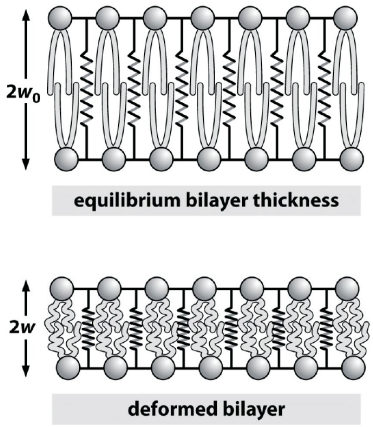

Figure 2.5: Illustration of the energetics of thickness deformations. (After Ref. [3].)

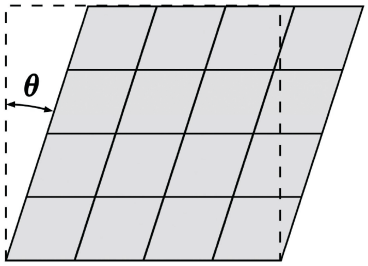

Figure 2.6: Schematic representation of shearing. (After Ref. [3].)

obtained in analogy to Hooke's law, which gives us

$$G_{\text{width}} = \frac{K_w}{2} \int dS \left(\frac{w - w_0}{w_0} \right)^2 , \tag{2.4}$$

where K_w has units of energy per unit area. A typical value for K_w is $K_w \approx 60 k_B T/\text{nm}^2$.

Shearing the membrane

As illustrated in Fig. 2.6, shear deformations displace the molecules which constitute a membrane relative to each other, while leaving the area per molecule unchanged. A membrane will only resist such a deformation if the relative positions of its constituent molecules are fixed by some lattice structure. Thus, fluid membranes are, by definition, unable to support shear deformations. But shear deformations can become relevant if the membrane is coupled to an external lattice structure such as the cytoskeleton [see Fig. 1.3(C)]. Since we only focus here on the most basic factors influencing membrane shape, we will not consider shear deformations in greater detail. However, in Sec. 3.3 we will consider the shapes of red blood cells, which can only be fully accounted for if, in addition to bending, shearing and stretching deformations are included. This provides an illustration of the general strategy of building on the most basic membrane deformations to gradually dissect the mechanisms driving a particular type of cell shape.

2.2 Bending energy

What type of membrane deformation determines the overall shape of vesicles and cells? The answer to this question clearly depends on the particular experimental system at hand, and on the energy scale we are interested in. Our focus will be on isolated vesicles with an energy scale set by the thermal energy. Thus, we first note that, in the absence of interactions with a cytoskeletal network, it will be possible to neglect shear deformations if the temperature is high enough for the membrane to be in its fluid state. Second, just as for a conventional fluid, we expect fluid membranes to strongly resist changes in overall volume. Thus, for perturbations brought about by thermal fluctuations, it should be possible to neglect effects related to area and thickness changes. These expectations are confirmed experimentally [7] by applying tension to membranes. This leaves us with bending as the likely candidate for the most basic type of membrane deformation. Much theoretical and experimental work has indeed confirmed that the shapes of vesicles can very well be described on the basis of the energetic cost associated with bending deformations, systematically adding in other types of deformations as dictated by the experimental system under consideration. In this section we will therefore discuss in greater detail the classic theory of bending, which is able to account for the basic phenomenology of vesicle and cell shapes.

As argued in the previous section, the simplest description of bending is given by Eq. (2.3). Several variants of this expression for the bending energy have been studied in the literature, with each variant incorporating the complexity of the underlying molecular interactions to a different degree. Below we will consider three classic versions of Eq. (2.3). But before embarking on a more detailed discussion of bending, let us mention an important mathematical result. The *Gauss-Bonnet theorem* states that

$$\int dSG = 4\pi(1-g)\,, \tag{2.5}$$

where the integer g is the genus of the surface, *i.e.*, the number of handles, and thereby characterizes the topology of the surface. For instance, a sphere has $g = 0$, whereas a torus has $g = 1$. Thus, if we assume that K_G is constant throughout the surface and only consider shapes of fixed topology, the bending energy will be independent of the Gaussian curvature. Changing the topology would require cutting the surface and, hence, would amount to a very strong perturbation of the system. This makes it very difficult to measure K_G, but also means that, in practice, it will be sufficient to restrict our attention to shape transformations which conserve a given topology. Thus, from now on we will neglect any contributions to the bending energy stemming from the Gaussian curvature.

Minimal model

From Eq. (2.3) and the Gauss-Bonnet theorem, the simplest description of bending is given by

$$G = \frac{K_b}{2}\int dSH^2\,, \tag{2.6}$$

where, for simplicity we have dropped the subscript "bend". The above form for the bending energy is expected to apply to lipid bilayers which consist of symmetric, homogeneous lipid monolayers.

Spontaneous curvature model

On a phenomenological level, we can include a potential asymmetry between the two monolayers constituting a bilayer membrane by assuming that there is a preferred mean curvature $H = C_0$. Thus, the expression for the bending energy is modified to

$$G = \frac{K_b}{2}\int dS(H-C_0)^2\,, \tag{2.7}$$

where C_0 is the *spontaneous curvature*. The expression for the bending energy in Eq. (2.7) is often referred to as the *Helfrich-Canham-Evans free energy of bending*. The microscopic meaning of C_0 is most easily understood by returning to the shape factor S defined in Sec. 1. In a lipid monolayer, we will only have $C_0 = 0$ for "cylindrical" lipids with $S \approx 1$. Similarly, a bilayer membrane will exhibit a spontaneous curvature if the two monolayers consist of lipids with different shapes. Another possible realization of spontaneous curvature is exposure of the two membrane leaflets to different chemical environments. Refinements of the spontaneous curvature model allow for membrane inhomogeneity, in which case the spontaneous curvature can vary along the surface and, indeed, couple to the surface shape.

Area-difference-elasticity model

The spontaneous curvature model recognizes that the two sides of the membrane may have different molecular compositions, but neglects any effects arising from the finite membrane thickness. In particular, depending on the curvature and the membrane thickness, it may be energetically favorable

to adjust the number of lipids on the two sides of the membranes which, in our coarse-grained representation of the system, corresponds to a change in relative membrane area. In order to find the difference in area between the two surfaces separated by a membrane width $2w$, consider two arcs of radius $R_1 - w$ and $R_1 + w$, respectively, where R_1 is one of the two principal radii of curvature. For small w, the ratio of the lengths of outer and inner arc is given by

$$\frac{R_1 + w}{R_1 - w} = 1 + 2\frac{w}{R_1} + \dots . \tag{2.8}$$

Repeating the same argument for the second principal radius of curvature, this gives us to leading order the value $1 + 2wH$ for the ratio of the areas associated with outer and inner leaflets, which is independent of the surface parameterization used. Thus, the total difference in area between outer and inner leaflets is given by

$$\Delta m = 2w \int dS H \,, \tag{2.9}$$

to leading order in w. Depending on microscopic interactions, Δm may or may not vanish for an unstressed system. Thus, assuming that deviations from the optimal value Δm_0 which correspond to stretching or compressing the two leaflets impose the same energy cost, we arrive at a bending energy of the form

$$G = \frac{K_b}{2} \int dS (H - C_0)^2 + \frac{K_b^\star \pi}{8Aw^2} \left(\Delta m - \Delta m_0\right)^2 \,, \tag{2.10}$$

where the nonlocal bending rigidity $K_b^\star$ can be related to the area stretch modulus. Thus, it has been argued on theoretical grounds that $K_b^\star / K_b$ may be of order unity. The spontaneous curvature C_0 in Eq. (2.10) can be absorbed into a redefined preferred area-difference Δm_0. The above model for the bending energy is referred to as the area-difference-elasticity (ADE) model.

2.3 Differential geometry of membranes

In this section we give a more precise mathematical definition to concepts such as "membrane shape" and "membrane curvature" on the basis of differential geometry. Differential geometry is the mathematical language appropriate for discussing the behavior of curved surfaces of arbitrary dimensions, embedded in spaces of arbitrary dimensions. As a result, differential geometry defines the (active or passive) "stage" on which physical phenomena play out, and is of general importance throughout science. However, implied by the general significance of differential geometry is also a high a degree of abstraction. While the abstract formulation of differential geometry, detached from any specific physical realization, is essential for the development of a powerful mathematical apparatus, it tends to obscure the implications of mathematical results for a specific physical system at hand. The aim of this section is to provide an introduction to the basic concepts of differential geometry relevant for membranes. In doing so, we will emphasize the connection to membranes as much as possible, but remind the reader that many more, potentially useful, results can be obtained from a more abstract treatment.

The concept of curvature

Before discussing the differential geometry of membranes, let us briefly review the concept of "curvature" in two-dimensional space. The curvilinear motion of an object in the x-y plane can be described, in parametric form, by a vector $\mathbf{r} = \mathbf{r}(s) = (x(s), y(s))$. In classical mechanics, $\mathbf{r}$ might describe the

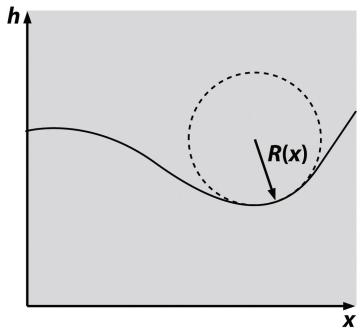

Figure 2.7: Osculating circle of a one dimensional curve. (After Ref. [3].)

motion of some object, in which case the variable s would denote time. The tangent vector, $\mathbf{t} = \mathbf{t}(s)$, along the curve is obtained by differentiating $\mathbf{r}(s)$,

$$\mathbf{t} = \mathbf{t}(s) = \frac{d}{ds}\mathbf{r} = \left(\frac{dx}{ds}, \frac{dy}{ds}\right) . \tag{2.11}$$

Thus, $\mathbf{t}$ smoothly follows the curve $\mathbf{r}$, and thereby provides the "link" between adjacent points. Viewed differently, if we imagine walking along the curve $\mathbf{r}$, $\mathbf{t}$ determines the *direction* in which we walk at each point. This suggests that we can obtain the *change in direction* by differentiating $\mathbf{t}$ which, in classical mechanics, corresponds to the acceleration of the object exhibiting curvilinear motion. Now, depending on the specific $\mathbf{r}$, $\mathbf{t}'$ will, in general, have components tangential and perpendicular to $\mathbf{t}$. The tangential component of $\mathbf{t}'$ provides a measure of the change in the magnitude of $\mathbf{t}$, while the perpendicular component provides a measure of the change in direction, which is most relevant for our purposes and will therefore be evaluated below.

First, note that in Sec. 2.2 we defined the curvature of a spherical object as the inverse of its radius R, a definition which is easily adapted to one-dimensional curves (see Fig. 2.7). The parametric representation of a circle with radius R and arc length $\bar{s}$, related to s by $\bar{s} = Ks$, is given by $\mathbf{r}_c(\bar{s}) = R(\cos\left(\frac{\bar{s}}{R}\right), \sin\left(\frac{\bar{s}}{R}\right))$. In order find the curvature along arbitrary $\mathbf{r}$, consider two points along the curve $\mathbf{r}$, separated by ds, with tangent vectors $\mathbf{t}$ and $\mathbf{t}_d$, respectively. Assuming that the two vectors subtend an angle $d\theta$, the component of the difference vector $\mathbf{t}_d - \mathbf{t}$ perpendicular to $\mathbf{t}$ is given by $t_d \sin d\theta$. Now, locally approximating $\mathbf{r}$ by $\mathbf{r}_c$, we have $d\theta = Kds/R$. Passing to the limit $ds \to 0$, this gives us

$$\left.\frac{d\mathbf{t}}{ds}\right|_{\text{normal}} = \lim_{ds\to 0} t_d \frac{\sin d\theta}{ds} = \lim_{ds\to 0} t_d \frac{d\theta}{ds} \overset{\text{(circle)}}{=} \frac{K^2}{R} , \tag{2.12}$$

where we have emphasized the step at which we locally approximate $\mathbf{r}$ by $\mathbf{r}_c$. Thus, if we use the same units for s and $\bar{s}$, which corresponds to $K = 1$, we can define the curvature

$$\frac{1}{R} \equiv \mathbf{n} \cdot \left(\frac{d^2\mathbf{r}}{ds^2}\right) \tag{2.13}$$

for arbitrary (differentiable) curves $\mathbf{r}$, where $\mathbf{n}$ is the unit normal vector perpendicular to $\mathbf{t}$.

Mathematical definition of surfaces

Membranes are two-dimensional objects embedded in three-dimensional space. Thus, we will focus on surfaces defined by

$$\mathbf{r} : \left(u^1, u^2\right) \mapsto \mathbf{r}\left(u^1, u^2\right) , \tag{2.14}$$

corresponding to a map from the two-dimensional surface parameterized by $\left(u^1, u^2\right)$ to the three-dimensional vector $\mathbf{r}$ which sweeps out the points on the surface. As for our one-dimensional curve, the tangent vectors are given by

$$\mathbf{e}_\mu = \mathbf{r}_{,\mu} := \frac{\partial \mathbf{r}}{\partial u^\mu} \,, \tag{2.15}$$

from which we obtain the unit surface normal vector

$$\mathbf{n} = \frac{\mathbf{e}_1 \times \mathbf{e}_2}{|\mathbf{e}_1 \times \mathbf{e}_2|} \,. \tag{2.16}$$

As an illustration of the above definitions, let us consider a particular representation of the mapping in Eq. (2.14) known as the *Monge parameterization*, in which we define a surface by its height h over some plane with orthonormal coordinates x and y. This representation of a surface is appropriate for surfaces with no overhangs and should, for instance, be contrasted with the description of a cylindrically symmetric surface in terms of cylindrical coordinates. For the Monge representation, the above definitions give[1]

$$\mathbf{r} = (x, y, h(x,y)) \,, \quad \mathbf{e}_x = (1, 0, h_x) \,, \quad \mathbf{e}_y = (0, 1, h_y) \,, \quad \mathbf{n} = \frac{1}{\left(1 + h_x^2 + h_y^2\right)^{1/2}} \left(-h_x, -h_y, 1\right) . \tag{2.17}$$

As can be seen from the above expressions, the x- and y-components of $\mathbf{n}$ vary with the change in h in the x- and y-directions, whereas the z component is fixed by the condition that $\mathbf{n}$ is a unit vector. Thus, as expected, if the surface is varying quickly in the x-direction, the magnitude of $\mathbf{n}$ will be dominated by its x-component, and *vice versa*.

The first and second fundamental form

Two quantities of paramount importance in differential geometry are the *first* and the *second fundamental form*, respectively. The *first fundamental form* or *metric* is the matrix defined by

$$g_{ij} := \mathbf{e}_i \cdot \mathbf{e}_j \,. \tag{2.18}$$

The name "metric" is inspired by the observation that the element of arc length squared is given by

$$(ds)^2 = \sum_{i,j=1}^{2} \left(\mathbf{e}_i du^i\right) \cdot \left(\mathbf{e}_j du^j\right) = \sum_{i,j=1}^{2} g_{ij} du^i du^j \,. \tag{2.19}$$

Moreover, we have

$$|\mathbf{e}_1 \times \mathbf{e}_2|^2 = |\mathbf{e}_1|^2 |\mathbf{e}_2|^2 \sin^2\phi = g_{11} g_{22} \left(1 - \cos^2\phi\right) = g_{11} g_{22} - \left(\mathbf{e}_1 \cdot \mathbf{e}_2\right)^2 = g_{11} g_{22} - g_{12} g_{21} = \det g \equiv g \,, \tag{2.20}$$

where we have used that, by virtue of the commutativity of the dot product, $g_{12} = g_{21}$. Thus, the area element of the surface, dS, is given by

$$dS = |\mathbf{e}_1 du^1 \times \mathbf{e}_2 du^1| = \sqrt{g} du^1 du^2 \,. \tag{2.21}$$

For the Monge parameterization, these definitions imply

$$g_{ij} = \begin{pmatrix} 1 + h_x^2 & h_x h_y \\ h_x h_y & 1 + h_y^2 \end{pmatrix} \,, \quad g = 1 + h_x^2 + h_y^2 \,. \tag{2.22}$$

[1] We neglect any subtleties related to the the notation for contravariant and covariant vectors appropriate for a more careful treatment.

In order to motivate the definition of the *second fundamental form*, let us return to our previous observation that, for a one-dimensional curve, the curvature is defined by $\frac{1}{R} \equiv \mathbf{n} \cdot \left(\frac{d^2\mathbf{r}}{ds^2} \right)$. For a point on a two-dimensional surface, we can define a local tangent plane through the vectors $\mathbf{e}_1$ and $\mathbf{e}_2$, which determine the local surface normal $\mathbf{n}$. Thus, there is an infinite number of two-dimensional planes which contain $\mathbf{n}$, and are therefore locally normal to the surface (see Fig. 2.4). Choosing a fixed but arbitrary normal plane, we are effectively dealing with a one-dimensional curve, determined by the surface contour within this particular normal plane, embedded in the two-dimensional normal plane. Again, we parameterize the curve by the variable s, *i.e.*, we let $\mathbf{r} = \mathbf{r}(s)$. For simplicity we focus on the Monge representation, in which case the chain rule of differentiation gives us

$$\frac{d\mathbf{r}}{ds} = \mathbf{r}_x \frac{dx}{ds} + \mathbf{r}_y \frac{dy}{ds} \,, \tag{2.23}$$

$$\frac{d^2\mathbf{r}}{ds^2} = \mathbf{r}_{xx} \left(\frac{dx}{ds} \right)^2 + \mathbf{r}_{yy} \left(\frac{dy}{ds} \right)^2 + \mathbf{r}_x \frac{d^2x}{ds^2} + \mathbf{r}_y \frac{d^2y}{ds^2} + 2\mathbf{r}_{xy} \frac{dx}{ds} \frac{dx}{ds} \,. \tag{2.24}$$

Because $\mathbf{r}_x = \mathbf{e}_x \equiv \mathbf{e}_1$ and $\mathbf{r}_y = \mathbf{e}_y \equiv \mathbf{e}_2$ are orthogonal to $\mathbf{n}$, we therefore find

$$\mathbf{n} \cdot \frac{d^2\mathbf{r}}{ds^2} = \mathbf{n} \cdot \left(\mathbf{r}_{xx} \left(\frac{dx}{ds} \right)^2 + \mathbf{r}_{yy} \left(\frac{dy}{ds} \right)^2 + 2\mathbf{r}_{xy} \frac{dx}{ds} \frac{dx}{ds} \right) \tag{2.25}$$

$$= \sum_{i,j=1}^{2} \left(\mathbf{n} \cdot \mathbf{e}_{i,j} \right) \frac{du^i}{ds} \frac{du^j}{ds} \,. \tag{2.26}$$

Note that all the information regarding the particular normal plane we have chosen is contained in the term $\frac{du^i}{ds} \frac{du^j}{ds}$. In other words, the term $\mathbf{n} \cdot \mathbf{e}_{i,j}$ is a property of the surface alone, and does *not* depend on the specific normal plane we have chosen. This motivates us to define the second fundamental form, b_{ij}, as the matrix

$$b_{ij} := \mathbf{n} \cdot \mathbf{e}_{i,j} \,. \tag{2.27}$$

In the Monge representation, b_{ij} is given by

$$b_{ij} = \frac{1}{\left(1 + h_x^2 + h_y^2 \right)} \begin{pmatrix} h_{xx} & h_{xy} \\ h_{yx} & h_{yy} \end{pmatrix} \,. \tag{2.28}$$

Note that the second fundamental form, just as the first fundamental form, is symmetric in its two indices.

The left-hand side of Eq. (2.25) is also referred to as the *normal curvature* κ_N to emphasize that it is the curvature associated purely with the surface, rather than the curvature of, *e.g.*, some curve defined on the surface (although, as noted before, κ_N *does* depend on the specific normal plane chosen). Using Eq. (2.19), it follows that

$$\kappa_N = \frac{\sum_{i,j=1}^{2} b_{ij} du^i du^j}{\sum_{i,j=1}^{2} g_{ij} du^i du^j} \,. \tag{2.29}$$

From Eq. (2.29) one can obtain the extremal curvatures of the surface by performing a variational calculation, with the result that there are two extremal curvatures, one minimum and one maximum, in directions of the surface which are orthogonal to each other. Thus, one obtains expressions for the mean and Gaussian curvatures for arbitrary surface shapes.

Instead of following the rigorous, but rather formal, treatment outlined above, we will motivate the definition of the mean and Gaussian curvatures in a more intuitive fashion. First of all, note that

our ultimate goal is to find quantities which provide a physical characterization of the curvature of a given surface. From Eq. (2.29), this means that they must only depend on

$$m_{ik} = \sum_{j=1}^{2} b_{ij} g_{jk}^{-1} \,, \tag{2.30}$$

where g_{jk}^{-1} is the inverse of g_{jk}. Moreover, any physical description of a surface must be *invariant under coordinate transformations* since, while the surface is a physical object, our description in terms of a particular coordinate system is not. This principle, if formulated somewhat more carefully, lies at the heart of a range of physical theories, such as the theory of relativity. Thus, whatever quantity we construct from m_{ik} must be invariant under transformations such as a rotation of the coordinate system. From linear algebra we know that, for a 2×2 matrix, there are two such quantities: the trace of the matrix, and its determinant. Now, the elements of the matrix m_{ik} have dimensions of inverse length, which means that $\mathrm{tr}\, m_{ik}$ also has dimensions of inverse length, whereas $\det m_{ik}$ has dimensions of inverse length squared. Thus, we associate $\mathrm{tr}\, m_{ik}$ with the mean curvature, and $\det m_{ik}$ with the Gaussian curvature, respectively. As for the case of a one-dimensional curve, we set any proportionality factors equal to 1, meaning that we use the same units for the radius of our (fictitious) circle and the surface arc length. Heuristically, we therefore arrive at the expressions

$$2H := \frac{1}{R_1} + \frac{1}{R_2} = \mathrm{tr}\, m_{ik} = \mathrm{tr} \left(\sum_{j=1}^{2} b_{ij} g_{jk}^{-1} \right) = \mathrm{tr} \left(\sum_{j=1}^{2} g_{kj}^{-1} b_{ji} \right) \,, \quad K := \frac{1}{R_1} \frac{1}{R_2} = \det m_{ik} = \frac{b}{g} \,, \tag{2.31}$$

where, as before, R_1 and R_2 are the two principal radii of curvature, and we have used that $\mathrm{tr}\,(AB) = \mathrm{tr}\,(BA)$ and $\det(AB) = \det(A)\det(B)$ for two square matrices A and B of the same order. The above result is confirmed by the derivation of H and K from Eq. (2.26). For the Monge representation, we therefore find

$$H = \frac{h_{xx}\left(1 + h_y^2\right) + h_{yy}\left(1 + h_x^2\right) - 2h_x h_y h_{xy}}{2g^{3/2}} \,, \tag{2.32}$$

$$K = \frac{h_{xx} h_{yy} - h_{xy}^2}{g^2} \,. \tag{2.33}$$

Chapter 3

Equilibrium shapes

This chapter shows how the theoretical concepts developed in the previous chapter can be applied to predict the shapes of vesicles and cells. In Sec. 3.1 we introduce the basic techniques generally used to find minimum energy shapes. Section 3.2 demonstrates how these techniques are employed to find the dominant vesicle shapes implied by bending deformations. Finally, in Sec. 3.3 we illustrate how these ideas can be applied to real cells by considering the shapes of red blood cells.

3.1 Minimization of membrane energy

On physical grounds we expect that vesicles will adopt the shape for which the energetic cost arising from membrane deformations is minimized. We thereby assume that nonequilibrium effects are small, *i.e.*, that the system is not perpetually driven away from its equilibrium state, and that the effects of thermal fluctuations can be neglected. The former assumption can be satisfied by constructing a sufficiently well-controlled environment for the experimental study of vesicles. The latter assumption, to which we will return in Sec. 4, generally holds because the moduli characterizing membrane deformations are large compared to the thermal energy scale set by k_BT. But this assumption will break down if several different shapes are in close competition for the minimization of energy, such as during budding. A further subtlety arises from the observation that bilayer vesicles are often not stable for an arbitrarily long time. However, on experimentally relevant time scales (which are generally in the range of a few hours) vesicles are stable and can be considered as residing in a well-defined constrained equilibrium.

Three distinct (but related) approaches have been employed [1] for the determination of the minimum energy shape of vesicles: (a) solution of the Euler-Lagrange equations for an appropriate expression for the free energy, (b) variational determination of minimum energy shapes within a reduced set of shapes, and (c) discretization of the surface by a lattice and numerical energy minimization. The most widely employed (and most general) approach for the minimization of vesicle energy relies on the Euler-Lagrange equations. The concepts underpinning this approach will be discussed below. A more detail exposition of these techniques, as well as appropriate references, can be found in Ref. [1].

Euler-Lagrange equations

For a general surface $\mathbf{r} = \mathbf{r}(u^1, u^2)$, the bending energy is given by $G = G[\mathbf{r}]$. The square brackets thereby remind us that G depends on a *function* describing the global vesicle shape, rather than a finite set of variables. From a mathematical perspective, this means that G is a *functional*, which can be viewed as the limit $N \to \infty$ of a function depending on N arguments. To see why this is the case for

vesicles, note that $G = \int du^1 du^2 f(\mathbf{r})$, where the function f may also depend on the various derivatives of $\mathbf{r}$ and includes any factors related to the metric of the surface. This expression means that, in order to find G, we must associate with each of the uncountably-infinite number of points (u^1, u^2) a value of the integrand. If this rule or *function*, encoded by f, is arbitrary, then G is a *functional*. Thus, the problem of finding equilibrium vesicle shapes amounts to the functional analogue of finding the minima of some function subject to given constraints.

In order to see how functional minimization is performed, let us consider the simple case of a functional $I = I[u(s)]$ which depends only on the scalar function[1] u. This will allow us to illustrate the basic concepts of functional minimization without the complications arising from the differential geometry of two-dimensional surfaces. We define I through

$$I[u(s)] = \int_{a_1}^{a_2} ds f(u(s), u'(s)) \,, \tag{3.1}$$

where we have assumed that the integrand depends on u and u' in order to be consistent with the paradigmatic case of functional minimization found in the physics literature. For membranes, the integrand will involve higher-order derivatives, but the corresponding functional minimization is performed following similar steps as presented here.

The extrema of I are found by taking its functional derivative which, in direct analogy to the derivative of a function, is defined by

$$\frac{\delta I[u(s)]}{\delta u(s)} := \lim_{\epsilon \to 0} \frac{I[u(s) + \epsilon \eta(s)] - I[u(s)]}{\epsilon} \,, \tag{3.2}$$

for some arbitrary function $\eta(s)$. Expanding $f(u(s), u'(s))$ as a Taylor series, one finds

$$f(u + \epsilon\eta, u' + \epsilon\eta') = f(u, u') + \epsilon \frac{\partial f}{\partial u}\eta + \epsilon \frac{\partial f}{\partial u'}\eta' + \dots \,, \tag{3.3}$$

and, thus,

$$\begin{aligned} \frac{\delta I[u(s)]}{\delta u(s)} &= \lim_{\epsilon \to 0} \int_{a_1}^{a_2} ds \frac{1}{\epsilon} \left[\epsilon \frac{\partial f}{\partial u}\eta + \epsilon \frac{\partial f}{\partial u'}\eta' + \dots \right] && (3.4) \\ &= \int_{a_1}^{a_2} ds \left[\frac{\partial f}{\partial u}\eta + \frac{\partial f}{\partial u'}\eta' \right] && (3.5) \\ &= \int_{a_1}^{a_2} ds \left[\frac{\partial f}{\partial u} + \frac{d}{ds}\frac{\partial f}{\partial u'} \right] \eta + \left[\frac{\partial f}{\partial u'}\eta \right]_{a_1}^{a_2} \,. && (3.6) \end{aligned}$$

The value of $\left[\frac{\partial f}{\partial u'}\eta\right]_{a_1}^{a_2}$ depends on the physical system under consideration. The simple scalar case which we discuss here is usually applied to situations where fixed boundary conditions are imposed at a_1 and a_2 (for instance, $u(s)$ may describe the height), in which case $u(s)$ cannot vary at $s = a_1, a_2$, and, hence, $\eta(a_1) = \eta(a_2) = 0$. Similarly, for a closed surface such as a vesicle, our integral must satisfy periodic boundary conditions, which implies that $\left[\frac{\partial f}{\partial u'}\eta\right]_{a_1}^{a_2} = 0$. Moreover, because η is arbitrary, the term in square brackets in Eq. (3.6) must vanish for arbitrary s. Thus, Eq. (3.6) reduces to

$$\frac{\partial f}{\partial u} + \frac{d}{ds}\frac{\partial f}{\partial u'} \,. \tag{3.7}$$

The above equation is referred to as the *Euler-Lagrange equation* for the functional I defined in Eq. (3.1). Given the ubiquity of standard differential calculus, it is not surprising that Euler-Lagrange equations appear throughout physics.

[1]The function $u(s)$ should not be confused with the variables u^1 and u^2 we use to parameterize surfaces.

Lagrange multipliers

If no constraints are imposed on our system, finding the vesicle shape amounts to the solution of the Euler-Lagrange equations appropriate for a two-dimensional surface. In practice, however, the shape of a vesicle must respect certain constraints such as conservation of vesicle volume or conservation of vesicle surface area. The above treatment can be expanded to include constraints *via* the method of Lagrange multipliers. To see how this works from a conceptual perspective, assume that our constraint is given by

$$J = \int_{a_1}^{a_2} ds g(u(s), u'(s)) = J_0 \,, \tag{3.8}$$

where J_0 takes some constant value corresponding, *e.g.*, to the total arc length in our one-dimensional example. As a result, the values of $u(s)$ are no longer independent in the interval $a_1 < s < a_2$, but must be chosen so that Eq. (3.8) is satisfied. This makes the corresponding minimization problem nonlocal and (seemingly) very hard to solve. But note that $\frac{\delta J}{\delta u} = 0$, which allows us to circumvent these difficulties by minimizing, instead of the functional I defined in Eq. (3.1), the functional

$$\int_{a_1}^{a_2} ds \left[f(u(s), u'(s)) + \lambda g(u(s), u'(s)) \right] \,, \tag{3.9}$$

where λ is called the *Lagrange multiplier*. Unless Eq. (3.8) is satisfied in a trivial way, *i.e.*, for arbitrary $u(s)$, the solution $\bar{u}(s)$ which minimizes Eq. (3.9) will depend on λ. This particular $\bar{u}(s)$ can then be substituted back into Eq. (3.8) to replace the unknown λ by the known J_0.

Thus, using the method of Lagrange multipliers, minimizing a functional under certain constraints simply amounts to solving a standard (unconstrained) minimization problem, followed by the evaluation of one integral for each constraint. This last step is often not even necessary since it is generally more convenient to work with an implicit definition of Lagrange multipliers. For the general case of N constraints to be imposed on a functional, N terms involving Lagrange multipliers are added to the functional to be minimized. Hence, functional calculus allows us, at least in principle, to find vesicle shapes for arbitrary deformation energies and an arbitrary number of constraints. In practice, the mathematical manipulations involved are too complicated to allow general solutions and it is necessary to focus on particular classes of shapes derived, *e.g.*, by perturbing a spherical shape, or axisymmetric shapes sweeped out by rotating an arbitrary non-intersecting curve around the symmetry axis, and to numerically solve the corresponding Euler-Lagrange equations. As a result, it is often useful to complement the above methodology by alternative methods such as the variational and computational approaches mentioned above.

3.2 Shapes with minimal bending energy

The combination of the minimization concepts discussed in the previous section and the theoretical principles developed in Sec. 2 has allowed the systematic exploration of vesicle and cell shapes from a theoretical point of view. Moreover, using bilayer vesicles, controlled experiments on cell shape can be performed. One common strategy is thereby to change the surface area of vesicles at a fixed volume by changing the temperature. This is made possible by different thermal expansion properties of lipid bilayers and the solutions in which they are embedded. Another common technique for the experimental analysis of bilayer vesicles is pipette aspiration, in which a pipette with micrometer diameter is used to probe the mechanical properties of vesicles. We will return to this technique in Sec. 4.

As argued in Sec. 2, the resistance of bilayers to area compression and area expansion is much larger than their resistance to bending deformations, while, in the fluid state, there is no resistance to

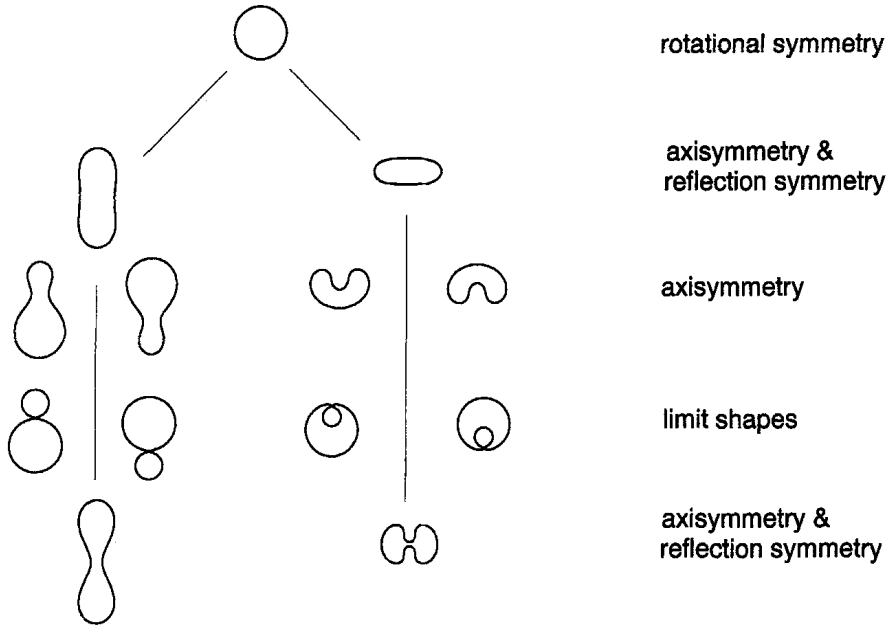

Figure 3.1: Typical axisymmetric equilibrium shapes of bilayer vesicles and their symmetries: sphere, prolate, oblate, pear-shape, stomatocyte, doublet, extreme stomatocyte, dumbbell, and a (discocyte) biconcave surface (top to bottom, left to right). (After Ref. [1].)

shear deformations. Thus, the most fundamental theory of vesicle shape is built on *minimization of bending energy*, subject to constraints appropriate for a particular experimental setup. The aim of this section is to summarize the vesicle shapes obtained within this most basic description of cell shape. Such an analysis can then serve as a starting point for the analysis of more complicated shapes, such as those of the red blood cells discussed in the next section.

Before embarking on a discussion of the vesicle shapes implied by the various models of bending considered before, it will be useful to preview the different classes of shapes we will encounter. Figure 3.1 shows the axisymmetric shapes of minimal bending energy obtained by breaking various symmetries of the sphere. Allowing for axisymmetry as well as reflection symmetry, one obtains prolate and oblate ellipsoids, which are defined by rotating an ellipse about its major and its minor axes, respectively. Following the shapes away from the sphere, one obtains dumbbells and biconcave surfaces. Breaking the up-down symmetry, pear shapes and stomatocytes bifurcate from prolates and oblates, respectively. Interesting limits of these shapes exhibiting a singular surface are the doublet and the extreme stomatocyte.

Minimal model

The simplest description of bending is given by the Helfrich-Canham-Evans model with zero spontaneous curvature. As mentioned in Sec. 2, for surfaces of fixed topology, the surface integral over the Gaussian curvature always gives the same constant, irrespective of shape. Thus, we are left with the bending energy

$$G = \frac{K_b}{2} \int dS H^2 \,. \tag{3.10}$$

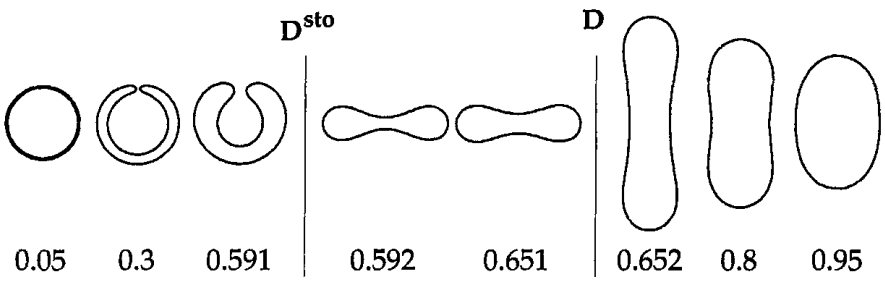

Figure 3.2: Symmetry classes of minimum energy shapes corresponding to the minimal model with increasing reduced volume: stomatocytes, oblates, and prolates (left to right). (After Ref. [8].)

As far as comparisons of the relative energies of vesicle shapes are concerned, the above description of vesicle shape is parameter free.

If no constraints are imposed on the vesicle under consideration, except that the surface must be free of intersections, the problem of finding the shapes minimizing Eq. (3.10) reduces to what is known as the "Willmore problem" in the mathematical literature. The solution to this problem depends on the topology of the surface, *i.e.*, the number of handles. For genus 0, which corresponds to spherical topology, it has been shown that the sphere is the unique solution to the Willmore problem. This means that, if no constraints such as fixed volume or fixed surface area are imposed, Eq. (3.10) implies that our vesicle will adopt the shape of a sphere. Increasing the genus of the surface, *i.e.*, adding a handle, we obtain a surface of toroidal topology. A possible solution to the Willmore problem for surfaces of genus 1 is the Clifford torus, which can be shown to be the shape of lowest G among all axisymmetric tori. For surfaces of higher genus, the solution to the Willmore problem is degenerate and, as a result, there are multiple shapes which minimize G. This has led to the prediction that vesicles of such a topology will continually change shape from one Willmore surface to another. Amazingly, this phenomenon, which is referred to as "conformal diffusion", has been observed experimentally. This gives strong support to energies based on Eq. (3.10) as an appropriate fundamental description of vesicles and cells.

Returning to the physically most relevant case of spherical topology, we note that, as mentioned above, experiments often probe vesicle shape by changing the surface area at fixed volume. By convention, the sequence of shapes is determined as a function of the reduced volume, v_{red}, defined as

$$v_{\mathrm{red}} = \frac{V}{(4\pi/3)R^3} \leq 1\,, \tag{3.11}$$

where the equality only holds for the sphere. Figure 3.2 summarizes the sequence of axisymmetric shapes with minimal energy obtained for the bending energy in Eq. (3.10) as a function of the reduced volume:

- $v_{\mathrm{red}} < v^a_{\mathrm{red}}$: Stomatocytes.
- $v^a_{\mathrm{red}} < v_{\mathrm{red}} < v^b_{\mathrm{red}}$: Oblates.
- $v^b_{\mathrm{red}} < v_{\mathrm{red}} < 1$: Prolates.

Here v^a_{red} and v^b_{red} are some characteristic values of the reduced volume. It is thought that the above sequence of shapes in fact represents the global energy minima for a given value of the reduced volume. Note that, because no pear shapes occur, the bending energy in Eq. (3.10) does not admit budding.

Spontaneous curvature model

The simplest description incorporating asymmetry between the two bilayers is given by a non-zero spontaneous curvature C_0, in which case our expression for the bending energy becomes

$$G = \frac{K_b}{2} \int dS(H - C_0)^2 \,. \tag{3.12}$$

Admitting a non-zero spontaneous curvature amounts to introducing a length scale C_0^{-1} into the system. As a result, the bending energy now depends on vesicle shape *and* vesicle size. Moreover, the sign of C_0 influences the cell shape such that a negative C_0 favors regions of negative curvature, and *vice versa*.

According to Eq. (3.12), the energies of vesicle shapes depend on the value of the spontaneous curvature in addition to the reduced volume. Thus, we need to expand our parameter space to two dimensions. Figure 3.3 summarizes the results of minimal energy calculations (and experiments) performed on the basis of Eq. (3.12). There are four large regions of axisymmetric shapes in parameter space. In addition to the prolates, oblates, and stomatocytes which were already found above with $C_0 = 0$, a positive C_0 can now also lead to a region in which pear shapes represent minima of the bending energy. Non-axisymmetric shapes have so far only been partially investigated on the basis of Eq. (3.12). Moreover, if the spontaneous curvature is generated by an inhomogeneous composition of either or both monolayers, we expect that lipid molecules will migrate to regions of curvature commensurate with their overall shape. In this interesting case already alluded to above, the energy minimization problem becomes considerably more involved.

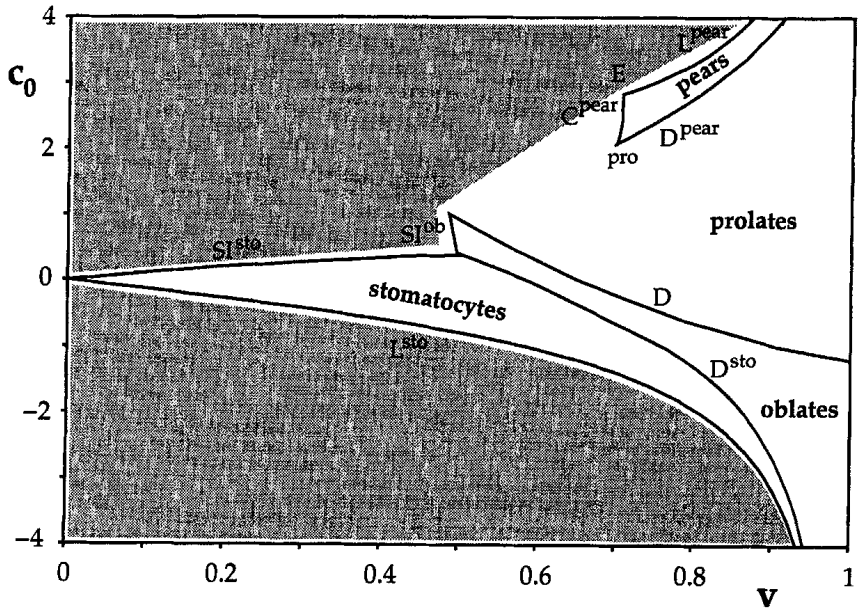

Figure 3.3: Minimum energy shapes of the spontaneous curvature model. (After Ref. [1].)

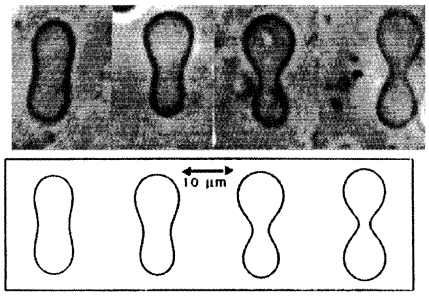

Figure 3.4: Experimentally observed vesicle shapes as in Fig. 1.5, and corresponding shapes predicted from theory for the same temperatures. (After Ref. [5].)

Area-difference-elasticity model

Finally, let us consider the situation where the two monolayers can have an area difference Δm. As seen before, this case is described by the ADE model with bending energy

$$G = K_b \left[\int dS (H - C_0)^2 + \alpha (\Delta m - \Delta m_0)^2 \right] . \tag{3.13}$$

While it can be shown that the set of stationary shapes of the ADE model is the same as for the spontaneous curvature model, the additional material parameters included in the ADE mean that the sequence of shapes will be different. It is found [1, 2] that shapes with more variations in their curvature become favorable as the value of Δm_0 is increased, which, from a microscopic perspective, may be viewed as adding excess lipids to the outer layer.

As illustrated by Figs. 3.2 and 3.3, Eq. (3.13) and its special cases allow the prediction of the vesicle shape for a particular set of parameters. How can these considerations be related to the shapes of real vesicles and cells? Given a particular cell shape, it will in general be possible (with some interesting exceptions which we will discuss in the next section) to determine the corresponding model parameters by fitting theoretical to experimental shapes. However, the choice of model will generally *not* be unique. In order to determine which model represents the "true" description of the vesicle or cell at hand, one can then experimentally vary parameters which, according to theory, are relevant for cell shape, such as the reduced volume or chemical differences on the two sides of the membrane. Different models will differ in their predictions regarding the outcome of such experiments. Thus, we can use this strategy to "weed out" models which do not capture the observed changes in cell shape. As an example, Figs. 3.4 and 3.5 show sequences of vesicle shapes predicted by appropriate variants of the ADE model for small changes in temperature (reduced volume). Agreement with the corresponding experimental shapes is obtained.

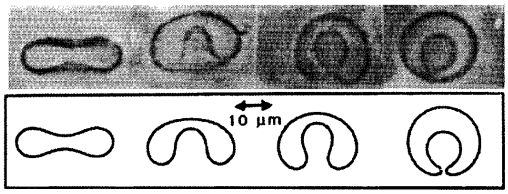

Figure 3.5: Experimentally observed vesicle shapes as in Fig. 1.6, and corresponding shapes predicted from theory for the same temperatures. (After Ref. [5].)

3.3 The shape of red blood cells

As illustrated in Sec. 1, red blood cells can adopt a variety of different shapes. We are now in a position to determine which features of these shapes can be accounted for from minimization of bending energy, and which (if any) require additional mechanisms. Under physiological conditions, red blood cells have a biconcave discoid (discocyte) shape (see Fig. 1.7 in Sec. 1). It is known experimentally that the shape of red blood cells can be systematically modified using two distinct sets of chemical reagents. One set of reagents (high pH, cholesterol enrichment, high salt, *etc.*) induces a series of shapes called echinocytes (see Fig. 1.7). But a second set of reagents (low pH, cholesterol depletion, low salt, *etc.*) produces a sequence of stomatocytes (see Fig. 1.7). This main sequence of shapes is universal in the sense that the order in which the different shapes appear does not depend on the specific chemical reagent used, only to which one of the two sets a particular reagent belongs.

As shown in the previous section, we are able to account for discocytes and stomatocytes on the basis of minimization of bending energy alone. However, echinocytes are not predicted by minimization of bending energy. This suggests that the shape transformations exhibited by red blood cells are driven, at least in part, by other types of membrane deformations. Indeed, from a biological perspective, one of the characteristic features of the membrane of red blood cells is the coupling of the membrane to an underlying cytoskeletal (spectrin) network. As a result, terms corresponding to shearing and stretching[2] must be considered in the overall energy budget. If these terms are included, the complete echinocytes–discocytes–stomatocytes sequence, as well as several shapes lying outside this main sequence, can be accounted for [6] by only varying the single parameter Δm_0. This suggests that the dominant effect of the two sets of reagents driving the shape of red blood cells is to increase or decrease Δm_0. Thus, biochemistry only comes into the picture on the level of coarse-grained, effective parameters, which provides a potential explanation for the apparent insensitivity of red blood cells to the underlying chemistry of reagents.

[2]The relevance of stretching results from the large deformations which are locally induced in some shapes competing with the shapes of the main sequence.

Chapter 4

Fluctuating membranes

While in the previous chapter we treated membrane shape as a static physical observable, experiments show that, not too surprisingly, the shape of membranes is fluctuating incessantly due to thermal excitations (see Fig. 4.1). In this chapter we will develop the basic theory of membrane fluctuations, which allows a quantitative understanding of how fluctuations affect the overall shape of vesicles and cells. Two important quantities characterizing membrane fluctuations are the correlation length and the amplitude of fluctuations, which are discussed in Secs. 4.1 and 4.2, respectively. Finally, in Sec. 4.3 we show how our theoretical understanding of membrane fluctuations can be used to measure basic membrane properties such as the membrane bending rigidity.

4.1 Surface correlation function

As discussed in Sec. 2, we represent the local orientation of a surface at position $\mathbf{r}$ by a unit normal vector $\mathbf{n} = \mathbf{n}(\mathbf{r})$. The scalar product $\mathbf{n}(\mathbf{r}_1) \cdot \mathbf{n}(\mathbf{r}_2)$ provides a measure of the surface fluctuations: For small separations $\Delta r = |\mathbf{r}_1 - \mathbf{r}_2|$ along the surface, we expect $\mathbf{n}(\mathbf{r}_1) \cdot \mathbf{n}(\mathbf{r}_2) \approx 1$, whereas, as we increase Δr, the surface normals will tend to become de-correlated, which means that $\mathbf{n}(\mathbf{r}_1) \cdot \mathbf{n}(\mathbf{r}_2)$ approaches zero and, for even larger Δr, may even become negative. The average $\langle \mathbf{n}(\mathbf{r}_1) \cdot \mathbf{n}(\mathbf{r}_2) \rangle$, taken over the entire surface and over all thermally excited surface configurations, therefore provides a quantitative measure of how "wavy" the surface is. Thus, $\langle \mathbf{n}(\mathbf{r}_1) \cdot \mathbf{n}(\mathbf{r}_2) \rangle$ is referred to as the *correlation function*

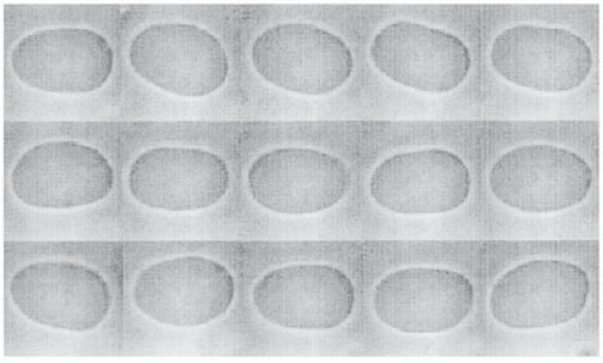

Figure 4.1: Time sequence of experimentally observed vesicle shapes, with an elapsed time of 6.3 s between subsequent frames. The vesicle fluctuates about an axisymmetric prolate shape, and the long axis has a length of approximately 20 μm. (After Ref. [9].)

of the surface. As we shall see, we have

$$\langle \mathbf{n}(\mathbf{r}_1) \cdot \mathbf{n}(\mathbf{r}_2) \rangle \propto \exp\left(-\frac{\Delta r}{\xi_p}\right) , \tag{4.1}$$

where ξ_p is the *correlation* or *persistence length* associated with a given surface. Thus, the correlation length provides a crucial measure of how much the surface shape is affected by thermal fluctuations. The aim of this section is to obtain an expression for ξ_p in terms of the fundamental physical parameters characterizing a membrane.

Transformation of $\langle \mathbf{n}(\mathbf{r}_1) \cdot \mathbf{n}(\mathbf{r}_2) \rangle$ to Fourier space

As shown in Sec. 2, we have $\mathbf{n}(\mathbf{r}) = (-h_x, -h_y, 1) \cdot (1 + h_x + h_y)^{-1/2}$ in the Monge parameterization of surfaces. For small surface deformations, we therefore obtain

$$\mathbf{n}(\mathbf{r}) = \left(-h_x, -h_y, 1 - \frac{1}{2}\left[h_x^2 + h_y^2\right]\right) + O\left(h_x^3, h_y^3\right) , \tag{4.2}$$

where we have used the result $(1+x)^n = 1 + nx + \ldots$ obtained *via* Taylor expansion. Equation (4.2) is the starting point for all calculations carried out in this chapter, and is correct up to quadratic order in h_x and h_y. A term $+O\left(h_x^3, h_y^3\right)$ is therefore implicit in all expressions to be derived, and we will return to the significance of higher-order terms below. Using the shorthand notation $h_{x,y;1,2} \equiv h_{x,y}(\mathbf{x}_{1,2})$, we find

$$\begin{aligned} \mathbf{n}(\mathbf{r}_1) \cdot \mathbf{n}(\mathbf{r}_2) &= h_{x;1}h_{x;2} + h_{y;1}h_{y;2} + 1 - \frac{1}{2}\left[h_{x;1}^2 + h_{y;1}^2\right] - \frac{1}{2}\left[h_{x;2}^2 + h_{y;2}^2\right] && (4.3) \\ &= 1 - \frac{1}{2}\left(h_{x;1} - h_{x;2}\right)^2 - \frac{1}{2}\left(h_{y;1} - h_{y;2}\right)^2 . && (4.4) \end{aligned}$$

We see from the above expression that the surface orientation at two points on the surface is the same if the derivatives of the height function at these points are the same. However, the correlation in the surface orientation decreases with increasing differences in the derivatives such that the symmetries $h \to -h$ and $(x, y) \to (-x, -y)$ are not violated.

Denoting the total membrane area by A, the Fourier transform $h(\mathbf{q})$ of the height function $h(\mathbf{x})$ is defined by

$$h(\mathbf{x}) = \frac{A}{(2\pi)^2} \int d\mathbf{q}\, e^{i\mathbf{q}\cdot\mathbf{x}} h(\mathbf{q}) , \tag{4.5}$$

where $\mathbf{q} = (q_1, q_2)$. From Eq. (4.5) we immediately find

$$h_{x;1} - h_{x;2} = \frac{A}{(2\pi)^2} \int d\mathbf{q}\, i q_x \left(e^{i\mathbf{q}\cdot\mathbf{x}_1} - e^{i\mathbf{q}\cdot\mathbf{x}_2}\right) h(\mathbf{q}) , \tag{4.6}$$

where q_x denotes the x-component of $\mathbf{q}$. Keeping in mind that $z^2 = z\, z^*$ for a complex number z, where the superscript $*$ denotes the complex conjugate, we therefore obtain

$$\left(h_{x;1} - h_{x;2}\right)^2 = \frac{A^2}{(2\pi)^4} \int d\mathbf{q} \int d\mathbf{q}'\, q_x q_x' \left(e^{i\mathbf{q}\cdot\mathbf{x}_1} - e^{i\mathbf{q}\cdot\mathbf{x}_2}\right) \left(e^{-i\mathbf{q}'\cdot\mathbf{x}_1} - e^{-i\mathbf{q}'\cdot\mathbf{x}_2}\right) h(\mathbf{q}) h^*(\mathbf{q}') . \tag{4.7}$$

In order to find the positional average, $\langle\cdot\rangle_{\mathrm{pos}}$, of the above expression, we note that, due to the symmetry of the surface in the x- and y-directions, only the relative distance $\Delta\mathbf{r}$ or, alternatively, $\Delta\mathbf{x} = \mathbf{x}_1 - \mathbf{x}_2$, enters the positional average. Thus, the positional average is obtained by applying the

operator $\frac{1}{A}\int d\mathbf{x}_1 d\mathbf{x}_2 \delta\left(\Delta\mathbf{x} - (\mathbf{x}_1 - \mathbf{x}_2)\right)$. Integrating the delta function over $\mathbf{x}_2$ amounts to replacing $\mathbf{x}_2$ by $\mathbf{x}_1 - \Delta\mathbf{x}$ and, thus, we find

$$\langle (h_{x;1} - h_{x;2})^2 \rangle_{\rm pos} = \frac{A}{(2\pi)^4} \int d\mathbf{x}_1 \int d\mathbf{q} \int d\mathbf{q}'\, q_x q_x' e^{i(\mathbf{q}-\mathbf{q}')\cdot\mathbf{x}_1} \left(1 - e^{-i\mathbf{q}\cdot\Delta\mathbf{x}}\right)\left(1 - e^{i\mathbf{q}'\cdot\Delta\mathbf{x}}\right) h(\mathbf{q}) h^*(\mathbf{q}')\,, \tag{4.8}$$

upon pulling out factors of $e^{i\mathbf{q}\cdot\mathbf{x}_1}$ and $e^{-i\mathbf{q}'\cdot\mathbf{x}_1}$ from the first and second brackets in Eq. (4.7), respectively.

In order to proceed, we note that, by definition of the Dirac delta function,

$$\delta(\mathbf{x}) = \frac{1}{(2\pi)^2} \int d\mathbf{x} e^{i\mathbf{q}\cdot\mathbf{x}}\,, \tag{4.9}$$

we have

$$\langle (h_{x;1} - h_{x;2})^2 \rangle_{\rm pos} = \frac{A}{(2\pi)^2} \int d\mathbf{q} \int d\mathbf{q}'\, q_x q_x' \delta(\mathbf{q} - \mathbf{q}') \left(1 - e^{-i\mathbf{q}\cdot\Delta\mathbf{x}}\right)\left(1 - e^{i\mathbf{q}'\cdot\Delta\mathbf{x}}\right) h(\mathbf{q}) h^*(\mathbf{q}') \tag{4.10}$$

$$= \frac{A}{(2\pi)^2} \int d\mathbf{q}\, q_x^2 \left(1 - e^{-i\mathbf{q}\cdot\Delta\mathbf{x}}\right)\left(1 - e^{i\mathbf{q}\cdot\Delta\mathbf{x}}\right) h(\mathbf{q}) h^*(\mathbf{q})\,. \tag{4.11}$$

Multiplying out the brackets, and using that $\cos x = \frac{1}{2}\left(e^{ix} + e^{-ix}\right)$, this finally gives us

$$\langle (h_{x;1} - h_{x;2})^2 \rangle_{\rm pos} = \frac{A}{(2\pi)^2} \int d\mathbf{q}\, q_x^2 \left(2 - 2\cos\mathbf{q}\cdot\Delta\mathbf{x}\right) h(\mathbf{q}) h^*(\mathbf{q})\,. \tag{4.12}$$

Returning to Eq. (4.4) and taking the thermal as well as the positional average, we therefore find

$$\langle \mathbf{n}(\Delta\mathbf{x})\cdot\mathbf{n}(\mathbf{0})\rangle = 1 - \frac{A}{(2\pi)^2} \int d\mathbf{q}\, \left(q_x^2 + q_y^2\right)\left(1 - \cos\mathbf{q}\cdot\Delta\mathbf{x}\right) \langle h(\mathbf{q}) h^*(\mathbf{q})\rangle_{\rm therm}\,, \tag{4.13}$$

where we use $\Delta\mathbf{x}$ rather than $\Delta\mathbf{r}$ to emphasize that this result was obtained in the Monge representation and, thus, only applies to surfaces with no overhangs.

Thermal average

In order to evaluate $\langle h(\mathbf{q}) h^*(\mathbf{q})\rangle_{\rm therm}$, we need to specify the energy cost associated with the fluctuations in $h(\mathbf{x})$. For future convenience, we will consider a membrane which is allowed to bend and is also set under a tension τ. The free energy of such a membrane is given by

$$G = \tau\left(\int dS - S_0\right) + \frac{K_b}{2}\int dS H^2\,, \tag{4.14}$$

where, for simplicity, we have used our most straightforward description of the bending energy. Tension opposes the creation of new contour area (*via* an increase in the inter-lipid spacing) relative to the reference area S_0 set by the projection of the membrane onto the x, y-plane. As mentioned before, we have $dS = (1 + h_x^2 + h_y^2)^{1/2} d\mathbf{x}$ in the Monge representation, and $H = h_{xx} + h_{yy}$ to leading order in h. Thus, we find that

$$G = \frac{\tau}{2}\int d\mathbf{x}\left(h_x^2 + h_y^2\right) + \frac{K_b}{2}\int d\mathbf{x}\left(h_{xx} + h_{yy}\right)^2\,. \tag{4.15}$$

As before, it will be convenient to transform Eq. (4.15) to Fourier space. For the surface tension, we obtain

$$\begin{aligned}
\frac{\tau}{2}\int d\mathbf{x}\left(h_x^2+h_y^2\right) &= \frac{\tau}{2}\int d\mathbf{x}\frac{A^2}{(2\pi)^4}\int d\mathbf{q}\int d\mathbf{q}'\left(q_xq_x'+q_yq_y'\right)e^{i(\mathbf{q}-\mathbf{q}')\cdot\mathbf{x}}h(\mathbf{q})h^*(\mathbf{q}') && (4.16)\\
&= \frac{\tau}{2}\frac{A^2}{(2\pi)^2}\int d\mathbf{q}\int d\mathbf{q}'\left(q_xq_x'+q_yq_y'\right)\delta(\mathbf{q}-\mathbf{q}')h(\mathbf{q})h^*(\mathbf{q}') && (4.17)\\
&= \frac{\tau}{2}\frac{A^2}{(2\pi)^2}\int d\mathbf{q}\,q^2h(\mathbf{q})h^*(\mathbf{q})\,, && (4.18)
\end{aligned}$$

where again we have used that $\delta(\mathbf{x})=\frac{1}{(2\pi)^2}\int d\mathbf{x}e^{i\mathbf{q}\cdot\mathbf{x}}$. Similarly, we find for the bending energy

$$\begin{aligned}
\frac{K_b}{2}\int d\mathbf{x}\left(h_{xx}+h_{yy}\right)^2 &= \frac{K_b}{2}\int d\mathbf{x}\frac{A^2}{(2\pi)^4}\int d\mathbf{q}\int d\mathbf{q}'\left(q_x^2+q_y^2\right)\left(q_x'^2+q_y'^2\right)e^{i(\mathbf{q}-\mathbf{q}')\cdot\mathbf{x}}h(\mathbf{q})h^*(\mathbf{q}') && (4.19)\\
&= \frac{K_b}{2}\frac{A^2}{(2\pi)^2}\int d\mathbf{q}\int d\mathbf{q}'\left(q_x^2+q_y^2\right)\left(q_x'^2+q_y'^2\right)\delta(\mathbf{q}-\mathbf{q}')h(\mathbf{q})h^*(\mathbf{q}') && (4.20)\\
&= \frac{K_b}{2}\frac{A^2}{(2\pi)^2}\int d\mathbf{q}\,q^4h(\mathbf{q})h^*(\mathbf{q})\,. && (4.21)
\end{aligned}$$

Thus, in Fourier space our expression for the energy in Eq. (4.15) reduces to the appealing form

$$G=\frac{A^2}{2(2\pi)^2}\int d\mathbf{q}\left(\tau q^2+K_bq^4\right)h(\mathbf{q})h^*(\mathbf{q})\,. \tag{4.22}$$

Based on the above expression for the total energy, we can now evaluate the thermal average over $h(\mathbf{q})h^*(\mathbf{q})$ by invoking the celebrated law of equipartition of energy: Each degree of freedom of a system, *i.e.*, each independent dynamic variable which is quadratic in the expression for the total energy, receives on average $\frac{1}{2}k_BT$ in thermal energy. The degrees of freedom of our surface are given by the $h(\mathbf{q})$ and, hence, we rearrange our expression for the total energy as

$$\langle G\rangle_{\text{therm}}=\frac{A}{(2\pi)^2}\int d\mathbf{q}\frac{A}{2}\left(\tau q^2+K_bq^4\right)\langle h(\mathbf{q})h^*(\mathbf{q})\rangle_{\text{therm}}\,, \tag{4.23}$$

where with each independent Fourier mode a wavenumber $\mathbf{q}$ is associated. Thus, the density of Fourier modes is given by $(2\pi)^2/A$ in Fourier space, and we have

$$\langle h(\mathbf{q})h^*(\mathbf{q})\rangle_{\text{therm}}=\frac{k_BT}{A\left(\tau q^2+K_bq^4\right)}\,. \tag{4.24}$$

As expected, $\langle h(\mathbf{q})h^*(\mathbf{q})\rangle$ increases with temperature but decreases with the total area available to fluctuations, and increasing tension and bending modulus.

Calculation of the correlation length

With the above results in hand, we are now ready to obtain a general expression for the correlation length. Substituting Eq. (4.24) into Eq. (4.13) we find

$$\langle\mathbf{n}(\Delta\mathbf{x})\cdot\mathbf{n}(\mathbf{0})\rangle=1-\frac{k_BT}{(2\pi)^2}\int d\mathbf{q}\frac{(1-\cos\mathbf{q}\cdot\Delta\mathbf{x})}{(\tau+K_bq^2)}\,. \tag{4.25}$$

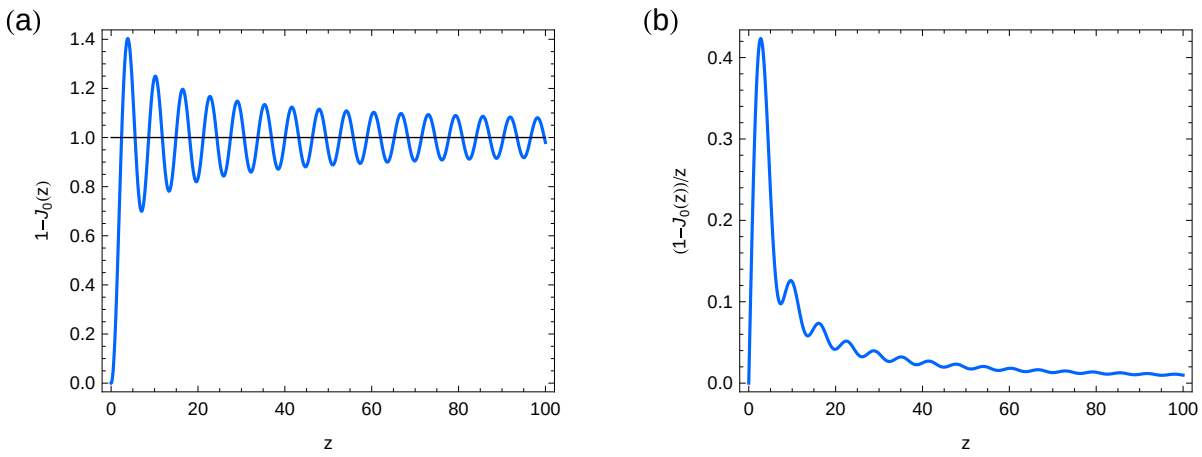

Figure 4.2: Plots of (a) $1 - J_0(z)$ and (b) $\frac{1-J_0(z)}{z}$ *versus* $z = q\Delta x$.

For a closed, unperturbed, and (meta-)stable vesicle, we have $\tau = 0$, and the above expression reduces to

$$\langle \mathbf{n}(\Delta\mathbf{x}) \cdot \mathbf{n}(\mathbf{0}) \rangle = 1 - \frac{k_B T}{(2\pi)^2 K_b} \int d\mathbf{q} \frac{(1 - \cos \mathbf{q} \cdot \Delta\mathbf{x})}{q^2} \,. \tag{4.26}$$

We proceed by transforming to polar coordinates and measuring angles relative to $\Delta\mathbf{x}$:

$$d\mathbf{q} = q\, dq\, d\theta \,, \quad \mathbf{q} \cdot \Delta\mathbf{x} = q\Delta x \cos\theta \,. \tag{4.27}$$

Thus, one finds

$$\langle \mathbf{n}(\Delta\mathbf{x}) \cdot \mathbf{n}(\mathbf{0}) \rangle = 1 - \frac{k_B T}{2\pi K_b} \int \frac{dq}{q} \left[1 - J_0(z)\right] \,, \tag{4.28}$$

where $z = q\Delta x$ and the Bessel function $J_0(z) \equiv \frac{1}{2\pi} \int_0^{2\pi} \cos(z \cos\theta)$ (see Fig. 4.2).

While, in principle, the limits of integration in the q-integral are 0 and ∞, we have, in practice, the upper cutoff π/b set by the intermolecular spacing b (see below). Moreover, noting that $\Delta x \geq b$, $\lim_{z\to 0} \frac{1-J_0(z)}{z} = 0$, and $\frac{1-J_0(z)}{z} = 1 - J_0(z) \approx 0.2$ for $z = 1$ (see Fig. 4.2), we approximate the lower cutoff by $1/\Delta x$. In this regime we can then set $1 - J_0(z) \approx 1$ and, thus, we find

$$\langle \mathbf{n}(\Delta\mathbf{x}) \cdot \mathbf{n}(\mathbf{0}) \rangle \approx 1 - \frac{k_B T}{2\pi K_b} \ln \frac{\pi \Delta x}{b} \,. \tag{4.29}$$

We can now define the correlation length ξ_p more precisely as the distance over which the correlation function decays to $1/e$,

$$1 - \frac{k_B T}{2\pi K_b} \ln \frac{\pi \xi_p}{b} \approx \frac{1}{e} \,, \tag{4.30}$$

which gives us

$$\xi_p \approx \frac{b}{\pi} e^{1.3\pi K_b / k_B T} \,. \tag{4.31}$$

The above result shows that the correlation length decreases (exponentially) with increasing temperature, which means that there will be fluctuations of shorter and shorter wavelength as the temperature is being increased. The scale for thermal fluctuations is set by the bending rigidity, which opposes

thermal fluctuations. Note that for the values $b \approx 1$ nm and $K_b \approx 10 k_B T$ typical for lipid bilayers, we obtain $\xi_p \approx 10^5$ km. This suggests that, as assumed in Sec. 3, in general there will be a well-defined overall vesicle shape on which thermal fluctuations merely act as a perturbation. Also note, however, that if we raise the temperature by approximately 10°K, our estimate for the correlation length decreases to $\xi_p \approx 20$ nm. This illustrates that, depending on the specific setup, fluctuations *can* be of great importance. For biological membranes, the bending rigidities typically reported are one order of magnitude higher than for pure lipid bilayers, with a corresponding increase in the expected correlation length for a given temperature.

In the calculation of the correlation length carried out above, we restricted ourselves to surfaces which can be described within the Monge representation, and only considered contributions to lowest order in h. The former assumption is justified in a self-consistent manner by our finding that, in general, the correlation length is very large compared to the vesicle size. Thus, membranes will be relatively smooth and, in particular, we can hope to be able to neglect interactions between opposite sides of the vesicle. However, when neglecting higher-order contributions in h, we ignored the possibility of interactions between different modes, *i.e.*, different length scales. Given that the spectrum of fluctuations, as well as the resistance to bending and tension, will depend on the length scale considered, it is not at all obvious that this assumption is justified. Interactions between different length scales can be accounted for by the renormalization group, which provides a systematic framework for integrating out and averaging over small scale degrees of freedom, and thereby relates the values of model parameters (or indeed general Hamiltonians) over different length scales. For our problem of calculating the persistence length, a renormalization-group calculation suggests that

$$\xi_p \sim b e^{4\pi K_b / 3 k_B T} \,, \tag{4.32}$$

which, in fact, is not too far from our estimate in Eq. (4.30). Moreover, the renormalization group also shows that quantities such as the bending rigidity are dependent on the length scale considered, as well as the temperature. Indeed, the bending rigidity is found to decrease linearly with the temperature, and logarithmically with the length scale.

4.2 Amplitude of fluctuations

The correlation length calculated in the preceding section characterizes how much the surface orientation is de-correlated along the surface contour by thermal fluctuations. Using the results obtained above, we can estimate the typical *amplitude* of fluctuations. As before, we will work in the Monge representation and consider only terms to lowest order in h. The quantity we wish to calculate is $\langle h(\mathbf{x})^2 \rangle$, where, as before, the angular brackets indicate an average over the surface and any thermal excitations of the surface. Applying the Fourier transform in Eq. (4.5), we find that

$$h(\mathbf{x})^2 = \frac{A^2}{(2\pi)^4} \int d\mathbf{q} \int d\mathbf{q}' \, e^{i(\mathbf{q}-\mathbf{q}')\cdot\mathbf{x}} h(\mathbf{q}) h^*(\mathbf{q}') \,. \tag{4.33}$$

Similarly as before, we apply the operator $\frac{1}{A}\int d\mathbf{x}$ to take the positional average of the above expression for a given surface configuration. Noting that $\delta(\mathbf{x}) = \frac{1}{(2\pi)^2}\int d\mathbf{x} e^{i\mathbf{q}\cdot\mathbf{x}}$, this leaves us with

$$\begin{aligned} \langle h(\mathbf{x})^2 \rangle_{\text{pos}} &= \frac{A}{(2\pi)^2} \int d\mathbf{q} \int d\mathbf{q}' \, \delta(\mathbf{q}-\mathbf{q}') h(\mathbf{q}) h^*(\mathbf{q}') & (4.34) \\ &= \frac{A}{(2\pi)^2} \int d\mathbf{q} \, h(\mathbf{q}) h^*(\mathbf{q}) \,. & (4.35) \end{aligned}$$

The thermal average of the above expression is found from Eq. (4.24), which means that

$$\langle h(\mathbf{x})^2 \rangle = \frac{k_B T}{(2\pi)^2 K_b} \int d\mathbf{q} \, \frac{1}{q^4} \, . \tag{4.36}$$

Transforming the above expression to polar coordinates, we find

$$\langle h(\mathbf{x})^2 \rangle = \frac{k_B T}{(2\pi)^2 K_b} \int_{\pi/A^{1/2}}^{\pi/b} dq \, \frac{2\pi q}{q^4} \, , \tag{4.37}$$

where, as before, we use the inverse maximal linear dimension and the inverse lipid spacing to approximate the lower and upper cutoffs on this momentum-space integral[1]. Thus, we find that

$$\langle h(\mathbf{x})^2 \rangle = \frac{k_B T}{4\pi K_b} \left[\left(\frac{A^{1/2}}{\pi} \right)^2 - \left(\frac{b}{\pi} \right)^2 \right] \approx \frac{k_B T}{4\pi^3 K_b} A \, . \tag{4.38}$$

As expected, the amplitude of fluctuations grows with temperature and the area accessible to fluctuations, but decreases with the bending rigidity. For the values $K_b \approx 10 k_B T$ and $A \approx 1 \ \mu m^2$, the above expression gives $\left(\langle h(\mathbf{x})^2 \rangle \right)^{1/2} \approx 100$ nm, or $\left(\langle h(\mathbf{x})^2 \rangle \right)^{1/2} \approx 300$ nm if the temperature is raised by 10°K from room temperature and the bending rigidity is kept fixed. This suggests that, as a very rough estimate, one expects amplitude fluctuations in biological membranes of the order of 100 nm over a lateral length scale of the order of 1 μm.

As an aside, we again note that we could have taken into account the coupling of different length scales by employing the renormalization group. In particular, the non-rigorous step of introducing *ad hoc* a lower (or, similarly, upper) cutoff in Eq. (4.37), necessary to prevent the divergence of the integral at $q = 0$, is a signature that we have not correctly accounted for the large-scale (and/or small-scale) behavior of the system. These difficulties are resolved by the renormalization group.

4.3 Measuring bending rigidity from thermal fluctuations

As found in Sec. 4.1, the presence of fluctuations at finite temperature means that the projected surface area of a membrane will generally be reduced relative to the corresponding contour surface area. For a tensionless membrane, we concluded that the strength of fluctuations and, hence, the reduction in area are governed by the dimensionless ratio of temperature and bending rigidity. If tension is applied to the membrane, thermal fluctuations will be "ironed out", and we expect the projected membrane area to increase. The aim of this section is to derive, based on the theory of fluctuating membranes presented above, a mathematical expression for the reduction in projected surface area, which will depend on the temperature, the bending rigidity, and the applied tension. Thus, we will see how one can measure the bending rigidity of a membrane by applying tension *via* measurement of the change in the projected membrane area, *i.e.*, the change in membrane fluctuations.

[1] More precisely, the motivation for this choice of limits comes from the solution of partial differential equations *via* Fourier series (see, *e.g.*, Ref. [10]): For a spatial interval $0 < x < A^{1/2}$, the possible wavenumbers are generally given by $k_n = \frac{n\pi}{A^{1/2}}$. Thus, $k \gtrapprox \frac{\pi}{A^{1/2}}$. The upper cutoff is obtained using the same argument but with $A^{1/2}$ instead of b. Now the minimal *prohibited* wavenumber is given by $k_1 = \frac{\pi}{b}$, meaning that the wavenumbers $k \gtrapprox \frac{\pi}{b}$ do not have physical significance.

Surface undulations

As shown in Sec. 4.1, the reduction in surface area of the projected surface is, to leading order in h, given by $\frac{1}{2}\int d\mathbf{x}\left(h_x^2+h_y^2\right)$ for a given surface configuration. Taking the thermal average and, as in Eq. (4.18), transforming to Fourier space, we find for the reduction in surface area, $A_{\rm r}$,

$$A_{\rm r}=\frac{1}{2}\int d\mathbf{x}\langle\left(h_x^2+h_y^2\right)\rangle=\frac{A^2}{2(2\pi)^2}\int d\mathbf{q}\,q^2\langle h(\mathbf{q})h^*(\mathbf{q})\rangle\,. \tag{4.39}$$

The thermal average in the above expression is again evaluated *via* Eq. (4.24), which we derived using equipartition of energy, leading to

$$A_{\rm r}=\frac{Ak_BT}{2(2\pi)^2}\int d\mathbf{q}\,\frac{1}{\tau+K_bq^2}\,. \tag{4.40}$$

The integrand in the above expression only depends on the absolute value of $\mathbf{q}$. Thus, upon transforming to polar coordinates and carrying out the (trivial) angular integration, we find

$$A_{\rm r}=\frac{A\pi k_BT}{(2\pi)^2}\int dq\,\frac{q}{\tau+K_bq^2}\,. \tag{4.41}$$

Changing the integration variable to $z=\tau+K_bq^2$ means that $qdq=\frac{1}{2K_b}dz$, leading to

$$A_{\rm r}=\frac{A\pi k_BT}{2K_b(2\pi)^2}\int\frac{dz}{z}\,. \tag{4.42}$$

As before, the physical description provided by the above integral is only valid in q between the lower and upper cutoffs $\pi/A^{1/2}$ and π/b, respectively. Thus, we find

$$A_{\rm r}=\frac{A\pi k_BT}{2K_b(2\pi)^2}\log\frac{\tau+K_b\frac{\pi^2}{b^2}}{\tau+K_b\frac{\pi^2}{A}}\,. \tag{4.43}$$

The above expression implies that $A_{\rm r}$ vanishes if $k_BT/K_b\to 0$, or $\tau/K_b\to\infty$; thermal fluctuations in the surface are suppressed by bending rigidity for zero temperature or infinite tension. But also note that these two limits are approached in a very distinct way, which we will exploit below.

Removing surface undulations by micropipette aspiration

In order to relate our expression for $A_{\rm r}$ to a quantity which can be measured experimentally, we need to specify a reference state relative to which changes in the projected surface area should be evaluated. Thermal fluctuations are most pronounced for $\tau=0$, which suggests that we use this region of parameter space to explore the relation between the bending rigidity of a given membrane and thermal fluctuations. Thus, we define the quantity

$$\Delta A\equiv\frac{A_{\rm r}(\tau=0)-A_{\rm r}(\tau>0)}{A} \tag{4.44}$$

$$=\frac{k_BT}{8\pi K_b}\log\left(\frac{A}{b^2}\frac{\tau+K_b\frac{\pi^2}{A}}{\tau+K_b\frac{\pi^2}{b^2}}\right)=\frac{k_BT}{8\pi K_b}\log\frac{\frac{\tau A}{K_b\pi^2}+1}{\frac{\tau b^2}{K_b\pi^2}+1}\approx\frac{k_BT}{8\pi K_b}\log\left(1+\frac{\tau A}{\pi^2K_b}\right)\,, \tag{4.45}$$

where, in the last step, we assumed that $\tau b^2\ll K_b$.

It is useful to briefly pause at this stage, and to reflect on the operational meaning of ΔA. Our definition of ΔA instructs us to first measure the projected surface area in the tensionless regime, to

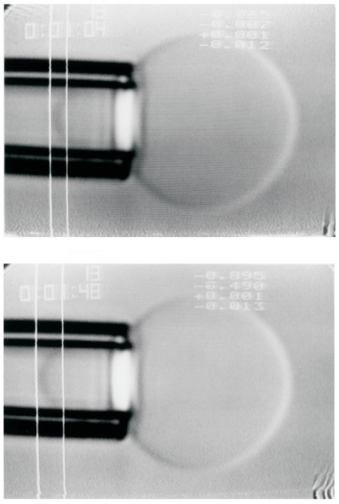

Figure 4.3: Videomicrographs showing an increase in apparent vesicle area by micropipette aspiration. The vesicle diameter is approximately 20 μm. With increasing tension the apparent surface area is found to increase by approximately 1 per cent (upper to lower panel). (After Ref. [11].)

repeat the measurement after a (small) tension has been applied, to take the difference between the two values for the projected area, and, finally, to divide the result by the contour area of the surface, A. Implicit in this procedure is that, first of all, the contour area *can* be measured, a point we will return to below. Second, we also assume that the contour area does not change as tension is applied to the surface (or as fluctuations perturb the surface), meaning that the expansion of the projected surface area due to increased tension is purely due to decreased surface area taken up by fluctuations. This is, of course, only a good assumption if the tension is small enough so that the spacing between lipid molecules does not increase appreciably. For large enough tension, this assumption will break down. In this regime, Eq. (4.45) must be modified to include membrane stretching, the membrane no longer fluctuates appreciably, and the modified version of Eq. (4.45) can then be used to measure the area-stretch modulus following a similar procedure as outlined here for the bending rigidity.

The experimental realization of the scenario described above is achieved through *micropipette aspiration measurements* (see Fig. 4.3). In these experiments, a small pipette, with diameter $d \approx 10\,\mu m$ or less, is used to probe vesicles or cells contained in a solution, with typical sizes of several micrometer. The pipette is connected to a pump, which allows the application of a known pressure difference between the pipette and the solution. Thus, vesicles can be "grabbed" and "held". Upon increasing the pressure difference, the bilayer is partially sucked into the inside of the pipette without rupturing it. Using video microscopy, it is then possible to characterize the shape of the deformed vesicles. On the basis of the known pressure difference, this allows [3] the calculation of the surface tension *via* the Laplace-Young law. Thus, it is possible to measure the tension and the surface area of the vesicle. If the surface area is large enough, Eq. (4.45) further simplifies to

$$\Delta A \approx \frac{k_B T}{8\pi K_b} \log \tau + C\,, \tag{4.46}$$

where we have absorbed all terms which do not depend on the surface tension into the term C. Measurement of ΔA as a function of $\log \tau$ will therefore give us a straight line with gradient $\frac{k_B T}{8\pi K_b}$. On this basis it is possible, for a known temperature, to experimentally measure the bending rigidity of lipid bilayers, which is the material parameter most crucial for the description of vesicle and cell shape developed in these notes.

Bibliography

[1] U. Seifert, Adv. Phys. **46**, 13 (1997).

[2] D. H. Boal, *Mechanics of the Cell* (Cambridge University Press, Cambridge, 2002).

[3] R. B. Phillips, J. Kondev, and J. Theriot, *Physical Biology of the Cell* (Garland Science, New York, 2009).

[4] L. Käs and E. Sackmann, Biophys. J. **60**, 825 (1991).

[5] K. Berndl, *et al.*, EPL **13**, 659 (1990).

[6] G. Lim H. W., M. Wortis, and R. Mukhopadhyay, Proc. Natl. Acad. Sci. **99**, 16766 (2002).

[7] E. Evans and D. Needham, J. Phys. Chem. **91**, 4219 (1987).

[8] U. Seifert, K. Berndl, and R. Lipowsky, Phys. Rev. A **44**, 1182 (1991).

[9] H.G. Döbereiner, E. Evans, M. Kraus, U. Seifert, and M. Wortis, Phys. Rev. E **55**, 4458 (1997).

[10] M. Boas, *Mathematical Methods in the Physical Sciences* (John Wiley & Sons, New York, 2nd ed., 1983).

[11] E. Evans and W. Rawicz, Phys. Rev. Lett. **79**, 2379 (1997).